THE JOURNAL OF BIOLOGICAL CHEMISTRY VOL. 292, NO. 6, pp. 2441–2456, February 10, 2017

Schwannomin-interacting Protein 1 Isoform IQCJ-SCHIP1 Is a Multipartner Ankyrin- and Spectrin-binding Protein Involved in the Organization of Nodes of Ranvier*◆

Received for publication, September 12, 2016, and in revised form, December 14, 2016 Published, JBC Papers in Press, December 15, 2016, DOI 10.1074/jbc.M116.758029

Pierre-Marie Martin[‡§¶1,2], **Carmen Cifuentes-Diaz**[‡§¶1], **Jérôme Devaux**[‖], **Marta Garcia**[‡§¶], **Jocelyne Bureau**[‡§¶], **Sylvie Thomasseau**[‡§¶], **Esther Klingler**[‡§¶3], **Jean-Antoine Girault**[‡§¶], **and Laurence Goutebroze**[§¶4]

From [‡]*INSERM, UMR-S 839, F-75005 Paris, the* [§]*Université Pierre et Marie Curie (UPMC)-Sorbonne Universités, UMR-S 839, 75005 Paris, the* [¶]*Institut du Fer à Moulin, 75005 Paris, and the* [‖]*Aix Marseille University, CNRS, CRN2M, 13344 Marseille, France*

Edited by Velia M. Fowler

The nodes of Ranvier are essential regions for action potential conduction in myelinated fibers. They are enriched in multimolecular complexes composed of voltage-gated Nav and Kv7 channels associated with cell adhesion molecules. Cytoskeletal proteins ankyrin-G (AnkG) and βIV-spectrin control the organization of these complexes and provide mechanical support to the plasma membrane. IQCJ-SCHIP1 is a cytoplasmic protein present in axon initial segments and nodes of Ranvier. It interacts with AnkG and is absent from nodes and axon initial segments of βIV-spectrin and AnkG mutant mice. Here, we show that IQCJ-SCHIP1 also interacts with βIV-spectrin and Kv7.2/3 channels and self-associates, suggesting a scaffolding role in organizing nodal proteins. IQCJ-SCHIP1 binding requires a βIV-spectrin-specific domain and Kv7 channel 1-5-10 calmodulin-binding motifs. We then investigate the role of IQCJ-SCHIP1 *in vivo* by studying peripheral myelinated fibers in *Schip1* knock-out mutant mice. The major nodal proteins are normally enriched at nodes in these mice, indicating that IQCJ-SCHIP1 is not required for their nodal accumulation. However, morphometric and ultrastructural analyses show an altered shape of nodes similar to that observed in βIV-spectrin mutant mice, revealing that IQCJ-SCHIP1 contributes to nodal membrane-associated cytoskeleton organization, likely through its interactions with the AnkG/βIV-spectrin network. Our work reveals that IQCJ-SCHIP1 interacts with several major nodal proteins, and we suggest that it contributes to a higher organizational level of the AnkG/βIV-spectrin network critical for node integrity.

Saltatory conduction in myelinated neurons depends on the compartmentalization of ion channels into polarized domains along the axons. Voltage-gated Na^+ (Nav)[5] and K^+ (Kv7.2/3) channels are clustered at axon initial segments (AIS) and nodes of Ranvier (NR), where they are responsible for the generation and propagation of action potentials and modulate axonal excitability. At NR and AIS, Nav and Kv7.2/3 are part of complexes, including cell adhesion molecules, NrCAM and neurofascin-186 (Nfasc186), and the scaffolding protein ankyrin-G (AnkG), which links membrane proteins to the underlying actin cytoskeleton through βIV-spectrin (1). Despite these molecular similarities, the mechanisms by which these complexes are concentrated are distinct at AIS and NR. Complex assembly at NR depends on both intrinsic axonal and extrinsic glial-controlled mechanisms, whereas AIS assembly depends only on intrinsic mechanisms (1). Several studies point to the ankyrin/spectrin network as a master organizer of both AIS and NR, controlling the molecular and nanoscale organization of the complexes and providing an elastic and stable mechanical support to the plasma membrane (1, 2). Mouse models highlight the essential role of βIV-spectrin in membrane stability (3–7).

SCHIP1 is a cytoskeleton-associated protein initially identified as a partner of schwannomin/merlin, the product of the tumor suppressor gene mutated in neurofibromatosis type 2 (NF2) (8, 9). No strong association between *SCHIP1* gene mutation and human nervous system disease has been reported with the exception of weak evidence for a possible link with autism spectrum disorders (10–13). In contrast, mutation of the *Drosophila* orthologue, Schip1, whose sequence is only poorly conserved, is embryonic lethal (14). In mammals, six different SCHIP1 isoforms, encoded by the same gene, are expressed in the nervous system (8, 15, 16). They differ by their N-terminal part and share a common C-terminal domain, including a leu-

* This work was supported by INSERM, Université Pierre et Marie Curie, and Fondation Orange Grant 14/2009, Fondation de France Grant 2009006047, Fondation pour la Recherche Médicale (FRM) Grant FDT20130928180, and by Agence Nationale pour la Recherche ANR-14-CE13-0011-02, EPI'K. The authors declare that they have no conflicts of interest with the contents of this article.

◆ This article was selected as one of our Editors' Picks.

[1] Both authors contributed equally to this work.

[2] Recipient of a doctoral fellowship from the Ministère de la Recherche et de l'Enseignement Supérieur, and a post-doctoral fellowship from the Association pour la Recherche sur la Sclérose en Plaques (ARSEP). Present address: Dept. of Psychiatry, University of California, San Francisco, CA 94158.

[3] Present address: Dept. of Basic Neurosciences, University of Geneva, 1211 Genova, Switzerland.

[4] To whom correspondence should be addressed: INSERM/UPMC UMR-S 839, Institut du Fer à Moulin, 17 Rue du Fer à Moulin, F-75005 Paris, France. Tel.: 33-1-45-87-61-44; Fax: 33-1-45-87-61-32; E-mail: laurence.goutebroze@inserm.fr.

[5] The abbreviations used are: Nav, voltage-gated Na^+; NR, node of Ranvier; AIS, axon initial segment; AnkG, ankyrin-G; BisTris, 2-[bis(2-hydroxyethyl)amino]-2-(hydroxymethyl)propane-1,3-diol; PH, pleckstrin homology; CH, calponin homology; SD, specific domain; CAP, compound action potential; IP, immunoprecipitation; Pnd, Paranodin; CV, conduction velocity; PNS, peripheral nervous system.

cine zipper region predicted to adopt a coiled-coil conformation. We previously showed that IQ-containing J protein-SCHIP1 (IQCJ-SCHIP1), an isoform with a specific N-terminal domain, is a component of AIS and NR (15). During development, IQCJ-SCHIP1 accumulates at NR and AIS after Nav channels and AnkG, indicating that it could play a role in the organization and stabilization of mature NR and AIS (15). IQCJ-SCHIP1 interacts directly with AnkG and is lost at AIS in the absence of AnkG (15). The interaction with AnkG requires the SCHIP1 C-terminal leucine zipper and phosphorylation by protein kinase CK2 (15, 17), which is enriched at NR and AIS, and regulates AnkG interactions with βIV-spectrin, Nav and Kv7 channels (17–20). IQCJ-SCHIP1 is absent from NR and AIS in quivering-3J mice (qv_{3J}) (15), which carry a mutation in the *Spnb4* gene encoding βIV-spectrin and lack Kv7.2 clustering at peripheral NR (21, 22). This suggests that IQCJ-SCHIP1 may associate with one or both of these proteins.

In this study we show that IQCJ-SCHIP1 is able to interact with both βIV-spectrin and Kv7.2/3 channels. Moreover, we provide evidence for IQCJ-SCHIP1 protein self-association, likely forming oligomers, suggesting a specific mechanism by which IQCJ-SCHIP1 participates in protein complex organization. We investigate the role of IQCJ-SCHIP1 *in vivo* by studying NR in peripheral myelinated fibers in *Schip1* mutant mice (*Schip1*Δ10, named hereafter Δ10), in which none of the six isoforms of SCHIP1 is expressed (16). We observe that the major nodal proteins, including AnkG, βIV-spectrin, and Kv7.2/3 channels, are normally present at NR in young and 14-month-old mutant mice, indicating that IQCJ-SCHIP1 is not required for their persistent nodal accumulation. However, Δ10 mice present an altered nodal shape similar to that observed in βIV-spectrin mutant mice, indicating that IQCJ-SCHIP1 contributes to nodal membrane-associated protein organization. Δ10 mice also display an increased accumulation of vesicles at NR as well as microtubule disorganization around mitochondria all along the axon, suggesting that SCHIP1 could play additional roles, possibly in relation with axon trafficking.

Results

IQCJ-SCHIP1 Interacts with βIV-Spectrin—Because IQCJ-SCHIP1 is absent from NR and AIS of qv_{3J} mice in which βIV-spectrin is mutated (15), we tested whether the two proteins can interact, using co-immunoprecipitation experiments from lysates of transfected COS-7 cells. Six βIV-spectrin alternative splice variants (Σ1–Σ6) were reported (7, 23, 24). Both βIVΣ1 and βIVΣ6 are enriched at NR (3). βIVΣ1 consists of an N-terminal calponin homology (CH) domain that binds actin and protein 4.1, 17 tandem spectrin repeats, a variable C-terminal region (specific domain (SD)), and a pleckstrin homology domain (PH) (Fig. 1*A*). βIVΣ6 is the shortest isoform and lacks the CH domain, 1–9 spectrin repeats, and part of spectrin repeat 10 (Fig. 1*A*). In qv_{3J} mutant mice, a single-base frameshift insertion in the SD domain of the *Spnb4* gene results in a 49-amino acid residue extension and the loss of the PH domain in both βIVΣ1 and βIVΣ6 (Fig. 1*A*) (21). Therefore, we investigated whether IQCJ-SCHIP1 interacted with βIVΣ6 and the protein domains involved in this interaction. Co-immunoprecipitations were first performed on lysates of cells expressing FLAG-tagged IQCJ-SCHIP1 (FLAG-IQCJ) and Myc-tagged βIVΣ6 (Myc-βIVΣ6). FLAG antibodies pulled down Myc-βIVΣ6 (Fig. 1*B*). Reciprocally, Myc antibodies pulled down FLAG-IQCJ (Fig. 1*C*). FLAG-IQCJ was, however, poorly detectable in co-immunoprecipitates from cells co-expressing a Myc-βIVΣ6 mutant protein with the qv_{3J} mutation (Myc-Σ6qv_{3J}) (Fig. 1*C*). This demonstrates that IQCJ-SCHIP1 interacts with βIVΣ6 and that this association is disrupted by the qv_{3J} mutation.

To identify more precisely the protein domains implicated in this interaction, we performed co-immunoprecipitations with βIVΣ6 proteins bearing various C-terminal deletions (see Fig. 1*A*). Deletion of either the PH and SD domains without (Myc-Σ6Δ1) or with deletion of part of the spectrin repeat 17 (Myc-Σ6Δ2) dramatically altered co-immunoprecipitation of FLAG-IQCJ (Fig. 1*C*). By contrast, FLAG-IQCJ was efficiently pulled down with a mutant βIVΣ6 protein lacking only the PH domain (Myc-Σ6Δ3) (Fig. 1*D*). These observations indicate that the interaction of βIV-spectrin with IQCJ-SCHIP1 requires its SD domain but not its PH domain. Interestingly and consistently, FLAG-IQCJ did not co-immunoprecipitate with GFP-tagged βII-spectrin (GFP-βII), which displays high sequence similarity with βIVΣ1 but does not contain an SD domain (Fig. 1, *A* and *E*) (23). We then performed reciprocal experiments, testing the ability of IQCJ-SCHIP1 to interact with various C-terminal parts of βIV-spectrin (see Fig. 1*F*). A molecule encompassing only part of the spectrin repeat 17 and the SD and PH domains (GFP-tagged, GFP-βIVCter) co-immunoprecipitated with FLAG-IQCJ (Fig. 1*G*), indicating that the C-terminal part of βIV-spectrin is sufficient for its association with IQCJ-SCHIP1. Co-immunoprecipitation was maintained or even increased when the PH domain was deleted (GFP-βIVSR-SD) or with the SD domain alone (GFP-βIVSD) (Fig. 1*G*). These results further support that the SD domain of βIV-spectrin is sufficient for the interaction and is the primary site of binding to IQCJ-SCHIP1, although a secondary binding site may exist within the spectrin repeat domain considering the low but consistent level of IQCJ-SCHIP1 binding to C-terminal truncated βIVΣ6 proteins (Fig. 1*C*, Myc-Σ6Δ1 and Myc-Σ6Δ2).

IQCJ-SCHIP1 Interacts with Kv7 Channels—We then examined whether IQCJ-SCHIP1 could interact with Kv7 channels, which are also absent from the peripheral NR of qv_{3J} mice (22). We carried out co-immunoprecipitation experiments on lysates of transfected COS-7 cells expressing FLAG-IQCJ and V5-tagged Kv7.2 or Kv7.3. V5 antibodies pulled down FLAG-IQCJ (Fig. 2*A*). Reciprocally, FLAG antibodies pulled down Kv7.2 or Kv7.3 (Fig. 3*C*), thus demonstrating that IQCJ-SCHIP1 is able to interact with both Kv7.2 and Kv7.3 channels.

We next performed mutations of Kv7 channel to identify the SCHIP1-binding domains. Kv7.2 and Kv7.3 encompass six transmembrane segments (S1–S6) and an intracellular C-terminal region comprising several structural subdomains including two calmodulin (CaM)-binding motifs (helices A and B), two tandemly arranged coiled-coils (helices C and D) implicated in dimerization/tetramerization, and an AnkG-binding motif (Fig. 2*B*) (25). FLAG-IQCJ did not co-immunoprecipitate with a Kv7.2 mutant lacking the intracellular C-terminal domain (Kv7.2-A306X) (Fig. 2*C*). However, FLAG-IQCJ was

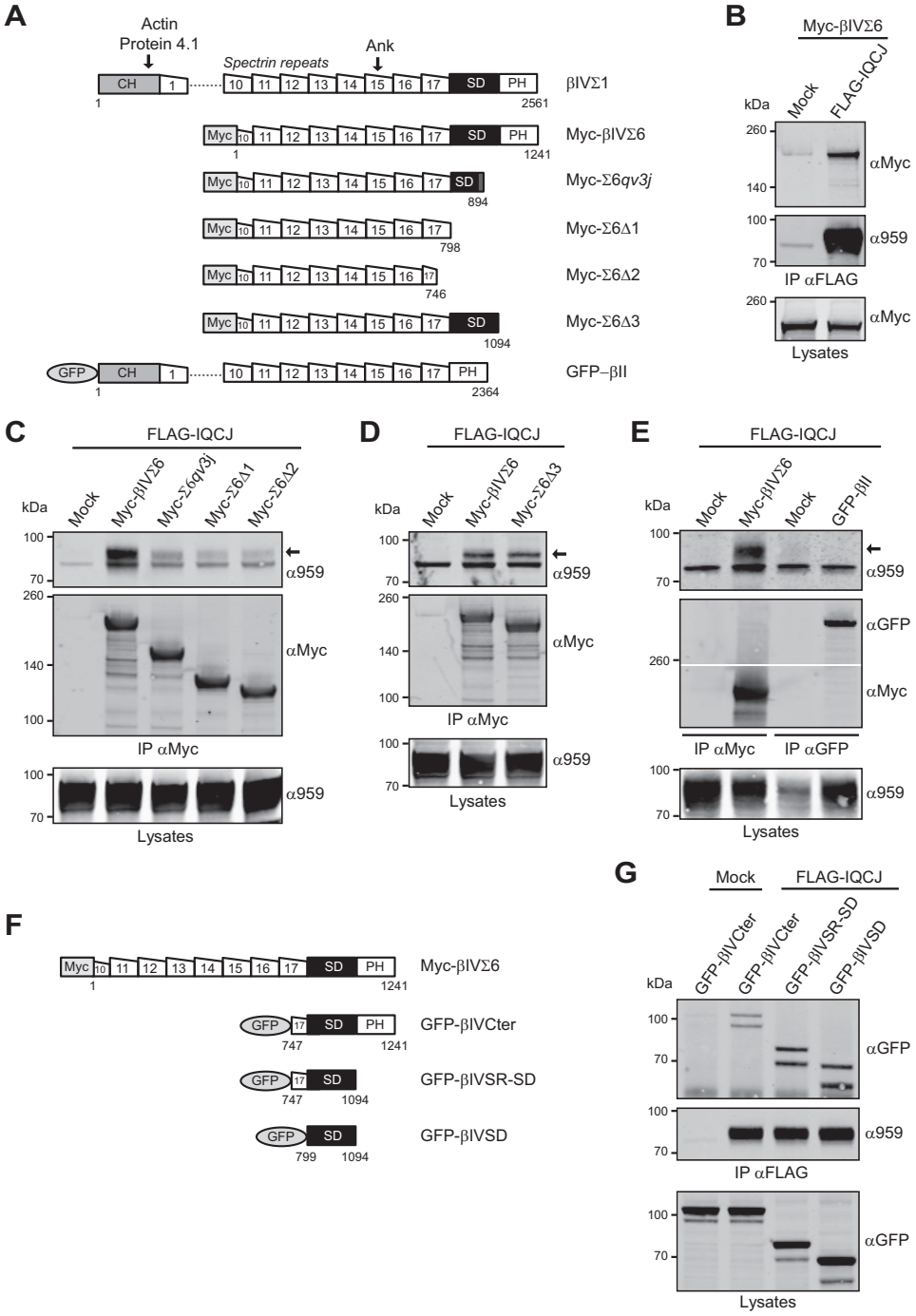

FIGURE 1. **Association of IQCJ-SCHIP1 and βIV-spectrin in transfected COS-7 cells.** *A*, schematic structural organization of βIVΣ1 spectrin, WT and mutant βIVΣ6 spectrin (Myc-tagged), βII-spectrin (GFP-tagged), and their interacting partners (*arrows*). *Dotted line* substitutes for spectrin repeats 2–9. *Numbers* correspond to amino acids. *B*, immunoprecipitation (*IP*) on lysates from COS-7 cells expressing FLAG-IQCJ and Myc-βIVΣ6 with FLAG antibodies and revealed by immunoblotting with Myc and SCHIP1 (α959) antibodies. Crude protein extracts (*Lysates*) were immunoblotted to verify protein expression. βIVΣ6 co-immunoprecipitates with FLAG-IQCJ. *C* and *D*, IP on lysates from cells expressing FLAG-IQCJ and WT or mutant Myc-βIVΣ6 proteins with Myc antibodies and revealed with Myc and α959 antibodies. FLAG-IQCJ co-immunoprecipitates with the mutant protein lacking the PH domain (Myc-Σ6Δ3) (*D*) but poorly with the mutant proteins presenting the qv_{3J} mutation (Myc-Σ6qv_{3J}) or lacking the PH and SD domains without (Myc-Σ6Δ1) or with deletion of part of the spectrin repeat 17 (Myc-Σ6Δ2) (*C*). *Arrows* indicate the position FLAG-IQCJ detected with the α959 antibody; the *lower band* is not specific. *E*, IP on lysates from cells expressing FLAG-IQCJ and Myc-βIVΣ6 proteins or GFP-tagged βII-spectrin (GFP-βII) with Myc or GFP antibodies and revealed with Myc, α959 and GFP antibodies. FLAG-IQCJ does not co-immunoprecipitate with GFP-βII. *F*, schematic structural organization of various C-terminal parts of βIV-spectrin (GFP-tagged) as compared with full-length Myc-tagged βIVΣ6 spectrin. *Numbers* correspond to amino acids. *G*, IP on lysates from cells expressing FLAG-IQCJ and various GFP-tagged C-terminal parts of βIV-spectrin with FLAG antibodies and revealed with GFP and α959 antibodies. FLAG-IQCJ pulls down a protein encompassing only part of the spectrin repeat 17 and the SD and PH domains (*GFP-βIVCter*). Co-immunoprecipitation is maintained when the PH domain is deleted (*GFP-βIVSR-SD*) or with the SD domain alone (*GFP-βIVSD*). *Mock*, transfection with an empty vector. Molecular mass markers are shown in kDa on the *left* of the panels.

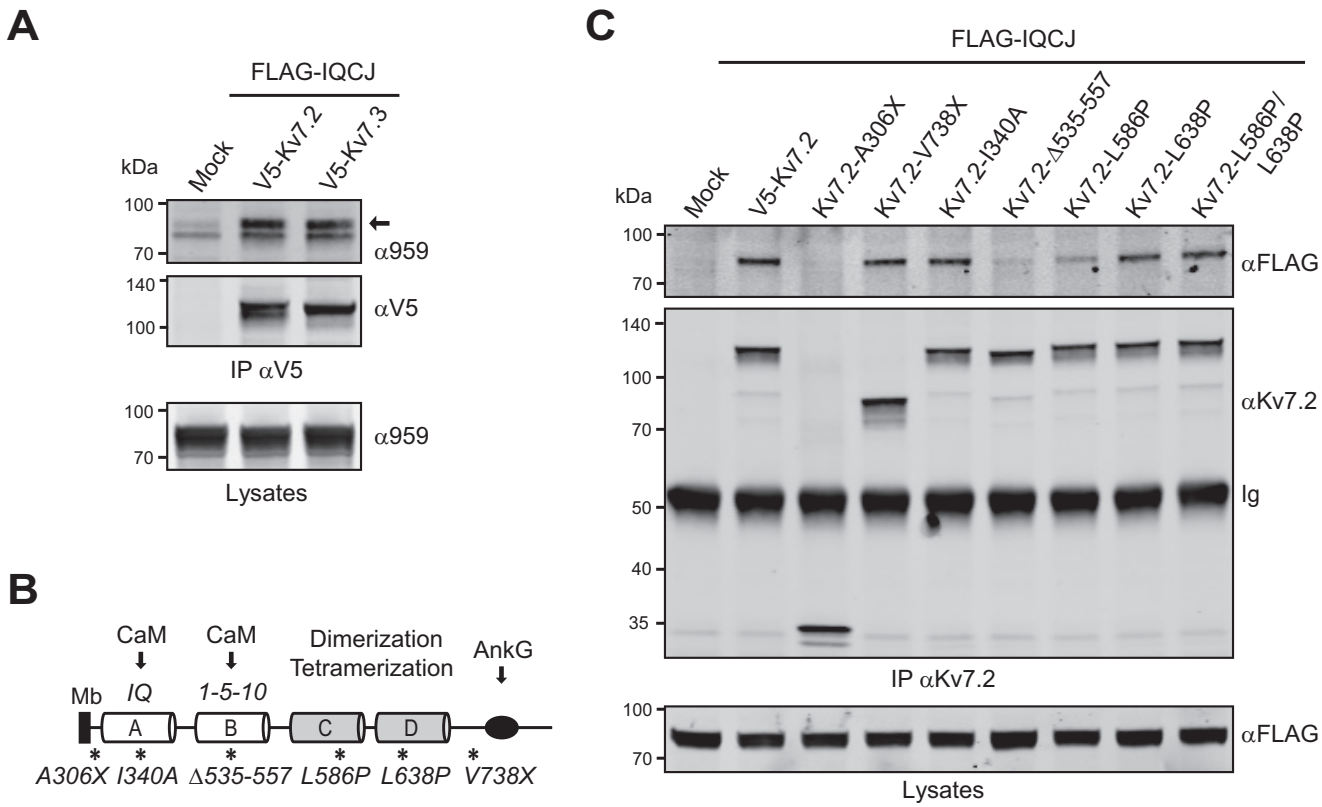

FIGURE 2. **Association of IQCJ-SCHIP1 and Kv7.2/Kv7.3 in transfected COS-7 cells.** *A,* IP on lysates from transfected COS-7 cells expressing FLAG-IQCJ and V5-Kv7.2 or V5-Kv7.3, with V5 antibodies, and revealed by immunoblotting with V5 and SCHIP1 (α959) antibodies. Crude protein extracts (*Lysates*) were immunoblotted to verify protein expression. V5 antibodies co-immunoprecipitate FLAG-IQCJ. The *arrow* indicates the position FLAG-IQCJ detected with the α959 antibody; the *lower band* is not specific. *B,* schematic structural organization of the C-terminal intracellular domain of Kv7.2 and position of the mutations or deletions (*). *Arrows* indicate the regions of interaction with AnkG and calmodulin (*CaM*). *A* and *B,* amphipathic α-helices containing the IQ and the two adjacent 1-5-10 consensus CaM-binding motifs, respectively; *C* and *D* indicate coiled-coils; *Mb*, plasma membrane. *C,* IP on lysates from cells expressing FLAG-IQCJ and WT or mutant Kv7.2 proteins, with Kv7.2 antibodies and revealed with FLAG and Kv7.2 antibodies. FLAG-IQCJ does not co-immunoprecipitate with Kv7.2 mutants deleted of the C-terminal intracellular domain (Kv7.2-A306X) or of the CaM binding 1-5-10 motif (*Kv7.2-Δ535–557*). *Mock*, transfection with an empty vector. Molecular mass markers are shown in kDa on the *left* of the panels.

pulled down with Kv7.2 mutants lacking the AnkG-binding domain (Kv7.2-V738X) or with point mutations that disrupt the CaM-binding IQ motif (Kv7.2-I340A) or dimerization/tetramerization (Kv7.2-L586P, Kv7.2-L638P, and Kv7.2-L586P/L638P) (Fig. 2*C*), although IQCJ-SCHIP1 pulldown was slightly reduced by the mutation L586P within the oligomerization coiled-coil domain. By contrast, FLAG-IQCJ association was strongly reduced by a mutation affecting the 1-5-10 consensus CaM-binding motif (Kv7.2-Δ535–557) (Fig. 2*C*), indicating that this motif is required for the interaction.

IQCJ-SCHIP1 Interactions Require Both C- and N-terminal Sequences—We then examined the IQCJ-SCHIP1 domains required for its interaction with βIV-spectrin and Kv7 channels by deleting the last 74 C-terminal residues encompassing the leucine zipper motif (FLAG-IQCJΔC) or the 325 N-terminal residues (FLAG-IQCJΔN) (Fig. 3*A*). Neither the C-terminal part of βIV-spectrin (residues 747–1241, HA-tagged, HA-βIVCter, Fig. 3*B*) nor Kv7.2 or Kv7.3 (Fig. 3*C*) co-immunoprecipitated efficiently with FLAG-IQCJΔN. Similarly, HA-βIVCter (Fig. 3*D*) and Kv7.2 and Kv7.3 (Fig. 3*E*) did not pull down FLAG-IQCJΔC. This indicates that the association of IQCJ-SCHIP1 with βIV-spectrin and Kv7 channels requires both its C-terminal coiled-coil region and more N-terminal sequences.

The specific 97-amino acid N-terminal domain of IQCJ-SCHIP1 contains an IQ CaM-binding motif , which is able to interact with CaM in the absence of a calcium (15). We further asked whether this domain was required for the association with HA-βIVCter and Kv7.2, using another SCHIP1 isoform, SCHIP1a (FLAG-1a), which presents a distinct 22-amino acid N-terminal domain (Fig. 3*A*). Both HA-βIVCter (Fig. 3*F*) and Kv7.2 (Fig. 3*G*) co-immunoprecipitated with FLAG-1a, indicating that the interactions of IQCJ-SCHIP1 with βIV-spectrin and Kv7 channels are not strictly dependent on its IQ CaM-binding motif but rather require sequences located between residues 97 and 325.

IQCJ-SCHIP1 Self-associates and Forms Oligomers—Requirement of the C-terminal coiled-coil region for both Kv7 and βIV-spectrin interactions was intriguing because we previously showed that this region was also required for SCHIP1 association with AnkG (15) and schwannomin (8). Of interest, bioinformatics analyses of the IQCJ-SCHIP1 amino acid sequence revealed a high content of potentially unfolded regions in the N-terminal and central domains and a higher probability of structuring at the C terminus, including the predicted coiled-coil region (Fig. 4*A*, *upper panel*). This coiled-coil region presented a high probability to form trimeric coiled-coils (Fig. 4*A*, *lower panel*), suggesting that IQCJ-SCHIP1 could

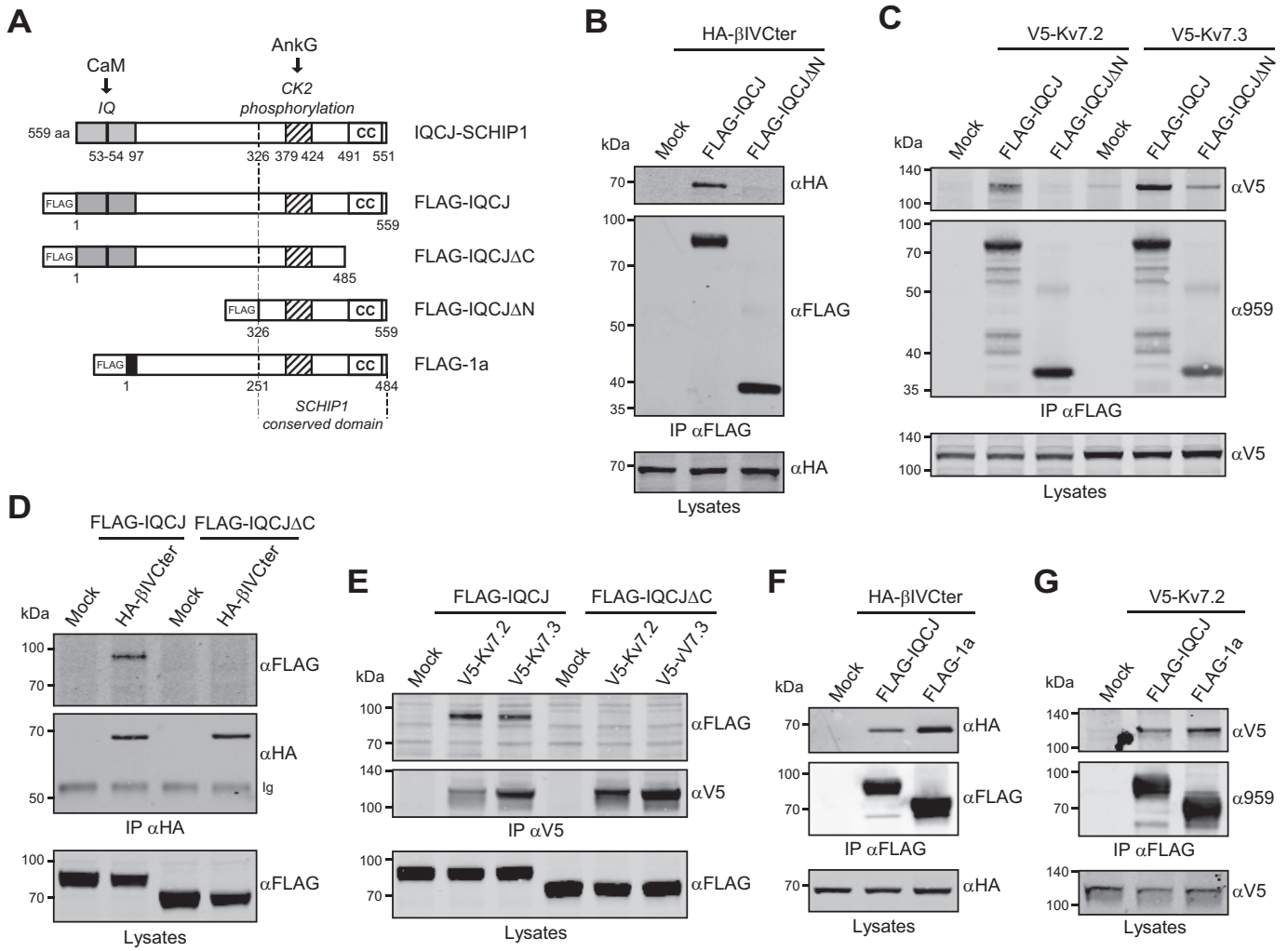

FIGURE 3. **IQCJ-SCHIP1 interactions required both C- and N-terminal sequences.** *A,* schematic structural organization of WT and mutant IQCJ-SCHIP1, SCHIP1a, and their interacting partners, calmodulin (*CaM*) and AnkG (*arrows*). *CC*, coiled-coil region; *IQ*, CaM-binding motif; *gray boxes*, specific 97-amino acids N-terminal domain of IQCJ-SCHIP1; *black box,* specific 22-amino acids N-terminal domain of SCHIP1a; *dashed boxes*, CK2 phosphorylation domain. *Numbers* correspond to amino acids. *Dashed lines* delineate the C-terminal domain, which is conserved in the six isoforms of SCHIP1 and found in almost all animals (annotated in Pfam as "*SCHIP-1 domain*," PF10148). *B,* IP on lysates from COS-7 cells overexpressing HA-βIVCter and FLAG-IQCJ or FLAG-IQCJΔN with FLAG antibodies and revealed by immunoblotting with HA and FLAG antibodies. Crude protein extracts (*Lysates*) were immunoblotted to verify protein expression. HA-βIVCter does not co-immunoprecipitate with FLAG-IQCJΔN. *C,* IP on lysates from cells overexpressing V5-Kv7.2 or V5-Kv7.3 and FLAG-IQCJ or FLAG-IQCJΔN with FLAG antibodies and revealed with V5 and SCHIP1 (α959) antibodies. V5-Kv7.2 or V5-Kv7.3 does not co-immunoprecipitate efficiently with FLAG-IQCJΔN. *D,* IP on lysates from cells overexpressing HA-βIVCter and FLAG-IQCJ or FLAG-IQCJΔC with HA antibodies and revealed with HA and FLAG antibodies. FLAG-IQCJΔC does not co-immunoprecipitate with HA-βIVCter. *Ig*, immunoglobulins. *E,* IP on lysates from COS-7 cells overexpressing V5-Kv7.2 or V5-Kv7.3 and FLAG-IQCJ or FLAG-IQCJΔC with V5 antibodies and revealed with V5 and FLAG antibodies. FLAG-IQCJΔC does not co-immunoprecipitate with V5-Kv7.2 or V5-Kv7.3. *F,* IP on lysates from cells overexpressing HA-βIVCter and FLAG-IQCJ or FLAG-tagged SCHIP1a (FLAG-1a) with FLAG antibodies and revealed with HA and FLAG antibodies. HA-βIVCter co-immunoprecipitates with FLAG-1a. *G,* IP on lysates from COS-7 cells overexpressing V5-Kv7.2 and FLAG-IQCJ or FLAG-1a with FLAG antibodies and revealed with V5 and α959 antibodies. V5-Kv7.2 co-immunoprecipitates with FLAG-1a. *Mock*, transfection with an empty vector. Molecular mass markers are shown in kDa on the *left* of the panels.

oligomerize. In support of this hypothesis, we had previously shown that SCHIP1 was able to self-associate *in vitro* (8). We thus wondered whether the C-terminal coiled-coil region could mediate IQCJ-SCHIP1 oligomerization *in vivo*. We first performed co-immunoprecipitation from lysates of COS-7 cells co-expressing HA-tagged IQCJ-SCHIP1 (HA-IQCJ) and FLAG-IQCJ or FLAG-IQCJΔC. HA antibodies pulled down FLAG-IQCJ but not FLAG-IQCJΔC (Fig. 4*B*), demonstrating the ability of IQCJ-SCHIP1 to self-associate through its coiled-coil region in a cell environment. We next analyzed cell lysates from transfected cells on native-polyacrylamide gels. Three protein bands (~150, ~440, and >1000 kDa) were detected for FLAG-IQCJ, whereas only one protein band (~140 kDa) was visible for FLAG-IQCJΔC (Fig. 4*C*). This observation supported the oligomerization of FLAG-IQCJ in cells through its coiled-coil region. Abnormal migration of FLAG-IQCJ and FLAG-IQCJΔC monomers (150/140 kDa *versus* 70/80 kDa on SDS-polyacrylamide gels) may be due to the high content of charged amino acids in IQCJ-SCHIP1 (~16.3% Glu/Asp). The ~440-kDa band may correspond to trimers, whereas the highest molecular band (>1000 kDa) indicates that IQCJ-SCHIP1 can form more complex oligomers. The interactions of IQCJ-SCHIP1 with its partners therefore may require its oligomerization rather than a direct interaction with its C-terminal domain. In addition, IQCJ-SCHIP1 might play a role in clustering together several proteins with which it interacts through its self-association.

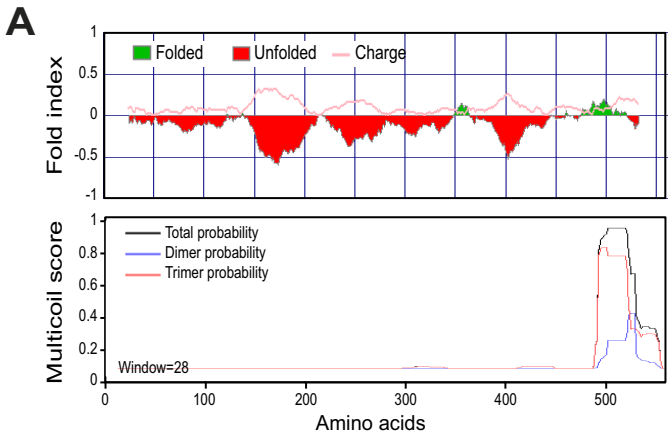

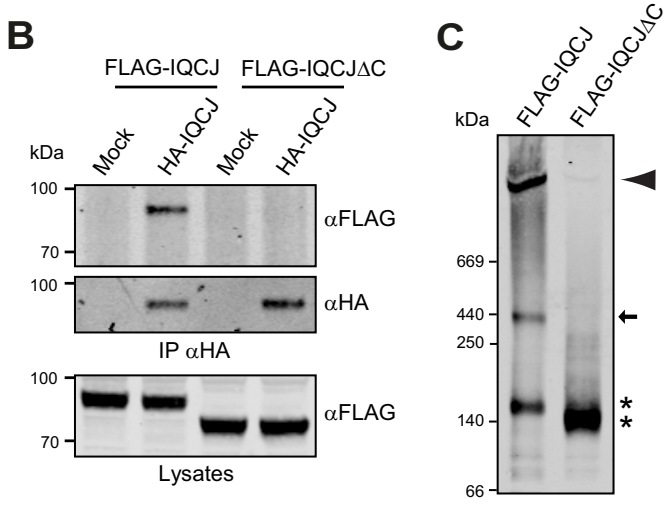

FIGURE 4. **IQCJ-SCHIP1 self-associates through its C-terminal domain.** *A,* probabilities of unstructured and charged regions (*upper panel*) and oligomerization (*lower panel*) along the mouse IQCJ-SCHIP1 amino acid sequence predicted with the FoldIndex and MULTICOILS software. *B,* IP on lysates from transfected COS-7 cells overexpressing HA-tagged IQCJ-SCHIP1 (HA-IQCJ) and FLAG-IQCJ or FLAG-IQCJΔC with HA antibodies and revealed by immunoblotting with FLAG and HA antibodies. Crude protein extracts (*Lysates*) were immunoblotted to verify protein expression. FLAG-IQCJ co-immunoprecipitates with HA-IQCJ, whereas FLAG-IQCJΔC does not. *C,* lysates from cells expressing FLAG-IQCJ or FLAG-IQCJΔC were resolved on native polyacrylamide gels and analyzed by immunoblotting with FLAG antibodies. Three proteins bands are detected for FLAG-IQCJ, whereas only one band is detectable for FLAG-IQCJΔC. * indicates the positions of FLAG-IQCJ and FLAG-IQCJΔC monomers (~140 kDa). The *arrow* indicates the band that may correspond to trimers (~440 kDa), and the *arrowhead* the band that may correspond to higher order oligomers (>1000 kDa). *Mock,* transfection with an empty vector. Molecular mass markers are shown in kDa on the *left* of the panels.

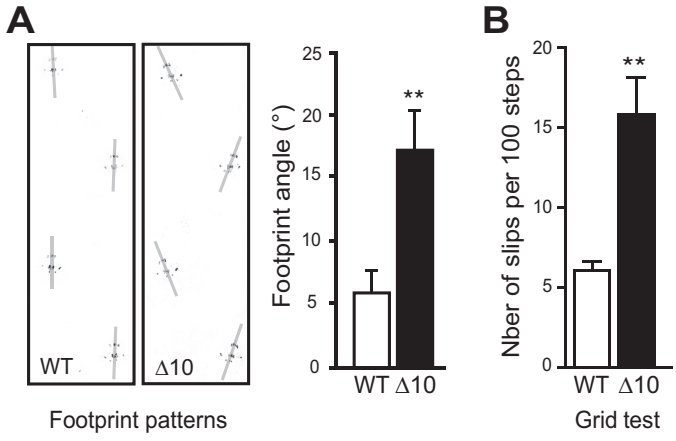

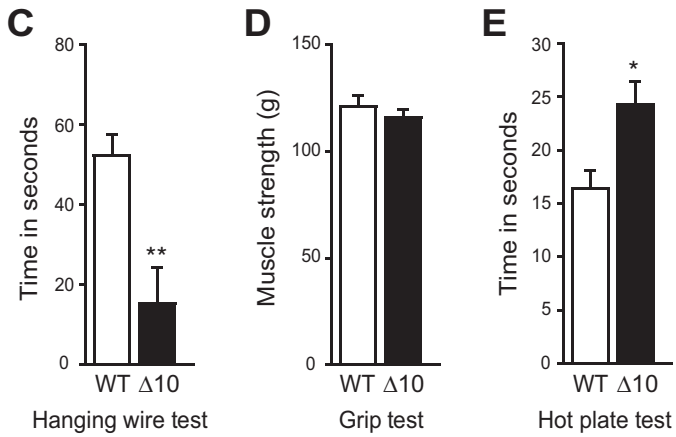

FIGURE 5. **Ataxia and hypoalgesia in Δ10 mice.** *A,* footprint test. Representative ink footprint patterns (*left panel*) revealed abnormal spreading of hind limbs for Δ10 mice (*right panel*). *Gray lines* on the *left panel* were drawn to measure footprint angles with regard to walking direction (three mice/genotype). *B,* grid test. When walking on a grid Δ10 mice slipped more often than WT mice (six mice/genotype). *C,* hanging wire test. The latency to fall down from the grid was significantly shorter for Δ10 mice than for WT mice (6–9 mice/genotype). *D,* grip strength analysis. The grip strength of Δ10 mice was similar to that of WT mice (7–9 mice/genotype). *E,* hot plate test. On a heated plate at 52 °C, paw withdrawal latency was increased for Δ10 mice compared with WT mice (7–9 mice/genotype). Data are means ± S.E. Statistical analyses: unpaired *t* test (*A–C*, **, $p < 0.01$; *D*, $p = 0.4643$, non significant; *E*, *, $p < 0.05$).

Δ10 Mice Display Locomotor and Sensory Dysfunctions—Altogether, our data showed that SCHIP1 associates with at least four nodal components as follows: AnkG, βIV-spectrin, and Kv7.2 and Kv7.3 channels. Our previous observations suggested that IQCJ-SCHIP1 could play a role in mature NR, potentially in NR organization and/or stabilization (15). We further explored SCHIP1 function in peripheral nerves by studying Δ10 mutant mice previously described, in which we showed that none of the six isoforms of SCHIP1 is expressed (16).

We first characterized the behavioral phenotype of Δ10 mice (4–6 months old), using a battery of tests that may indicate peripheral deficits. Although mice moved around normally in their home cages, footprint pattern analysis revealed subtle walking problems, including abnormal hind limb spreading (Fig. 5*A*). Tests of motor ability function such as grid test (Fig. 5*B*) and hanging wire test (Fig. 5*C*) also revealed impairments. However, the muscular strength of Δ10 mice evaluated by the grip test did not show any deficit (Fig. 5*D*). An increased reaction time was observed when mice were placed on a hot plate (Fig. 5*E*), indicating a slightly reduced pain sensitivity. Thus, mutant mice displayed some degree of ataxia and reduced pain sensitivity, which could reflect sensory defects.

Alterations of PNS Myelinated Fibers in Δ10 Mice—Behavioral deficits in mutant mice suggested peripheral nerve defects, although a central nervous system origin cannot be excluded because Δ10 mice also present some brain defects (16). We thus investigated peripheral nerve functions and morphology of Δ10 mice. Electrophysiological measurements showed that sciatic nerve conduction was not significantly different between mutant and wild-type (WT) littermates (Fig. 6*A*; Table 1;

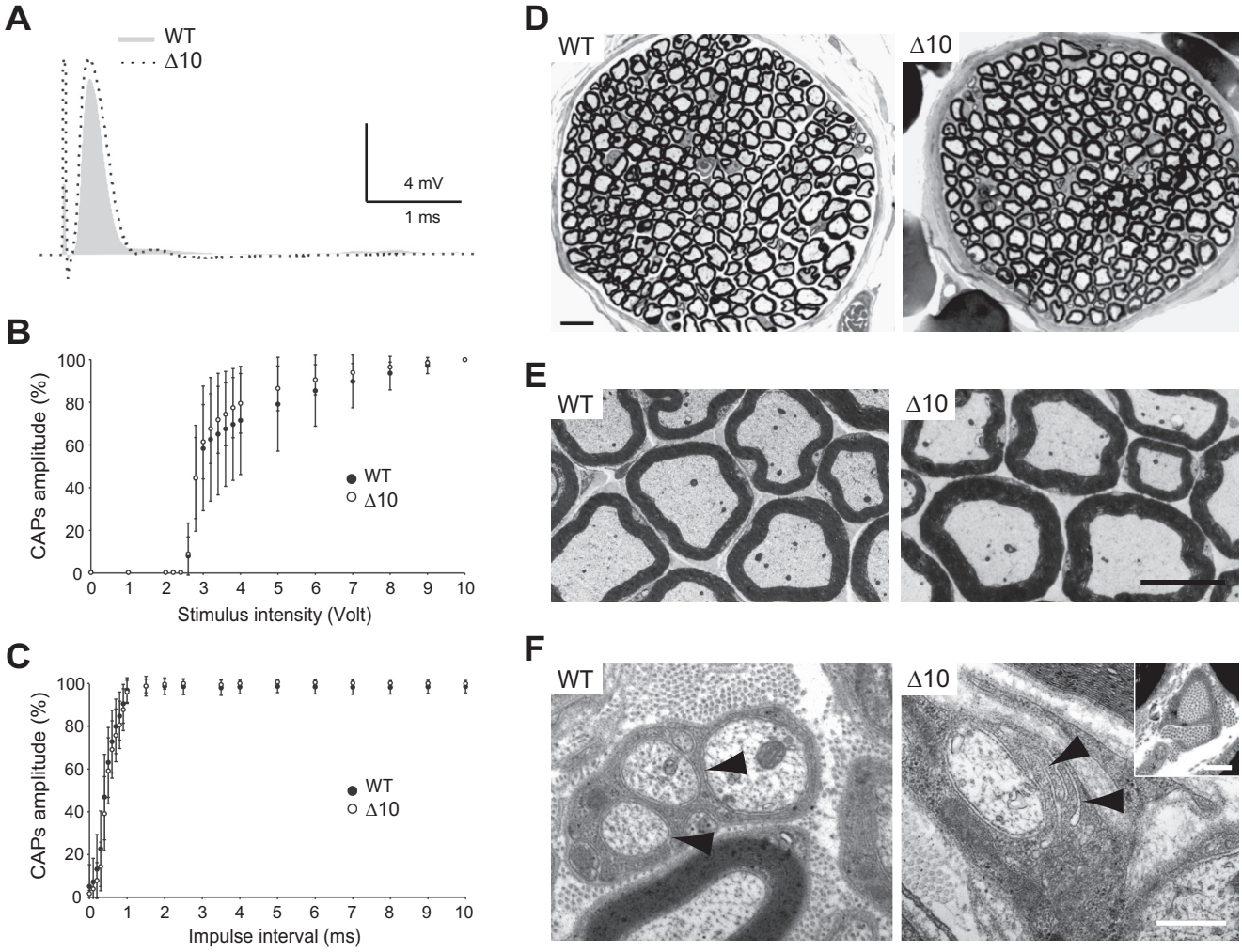

FIGURE 6. **Electrophysiological characteristics of sciatic nerves and structural abnormalities in phrenic nerves from Δ10 mice.** *A,* representative CAP recorded from sciatic nerves of 8-month-old WT and Δ10 mice (4–5 mice/genotype; 8–9 nerves/genotype). The trace is a superposition of the WT (*gray line*) and Δ10 (*dashed line*) CAP recordings. *B* and *C,* recruitment (*B*) and refractory period (*C*) of sciatic nerve axons. The *error bars* represent standard deviation. *D,* representative transversal semi-thin sections of phrenic nerves of 10-month-old WT and Δ10 mice (three mice/genotype). *E,* low magnification electron micrographs showing an apparent hypermyelination of the fibers in Δ10 mice compared with WT littermates. *F,* electron micrographs from phrenic nerve sections showing in Δ10 mice Schwann cell processes making several turns around small caliber axons (*arrowheads*), and collagen pockets in-between myelinated fibers (*inset*). In WT mice, several unmyelinated fibers are surrounded by a single Schwann cell (*arrowheads*). *Scale bars, D,* 8 μm; *E,* 5 μm; *F,* 0.5 μm.

TABLE 1

Electrophysiological characteristics of sciatic nerves of WT and Δ10 mice

$CV_{V,\,max}$ and $CV_{V,\,½}$ indicate conduction velocity at maximal amplitude and at half-maximal amplitude, respectively. The duration was measured at half the maximal amplitude. *n* represents the number of nerves tested. Data are means ± S.D. Statistical analyses: two-tailed *t* tests for two samples of equal variance. *, $p < 0.01$.

	WT	Δ10
A-fibers		
Amplitude (mV)	8.7 ± 2.9	11.3 ± 2.8
Area (mV·ms)	1097 ± 418	1732 ± 460
Duration (ms)	0.24 ± 0.02	0.28 ± 0.03*
$CV_{V,\,½}$ ($m·s^{-1}$)	71.3 ± 7.6	68.8 ± 5.3
$CV_{V,\,max}$ ($m·s^{-1}$)	48.7 ± 4.7	45.5 ± 2.7
C-fibers		
Amplitude	0.62 ± 0.25	0.73 ± 0.47
CV ($m·s^{-1}$)	0.86 ± 0.15	0.83 ± 0.10
n	8 (4 mice)	9 (5 mice)

8-month-old mice). CAPs duration was slightly increased in mutant mice but was not reflective of conduction defects. The recruitment (Fig. 6*B*) and the refractory period (Fig. 6*C*) of the CAPs were virtually identical in both genotypes. Also, the electrophysiological characteristics and the recruitment of the C-fiber component were not significantly different (Table 1).

Examination of semi-thin transversal sections of phrenic nerves (Fig. 6*D*) revealed a significant decrease of fiber number in Δ10 as compared with WT mice (WT, 241 ± 7.2; Δ10, 191.3 ± 7.9; mean ± S.E., $n = 3$ mice/genotype; unpaired *t* test, $t = 4.643$, **, $p < 0.01$; 10 month-old mice). In addition, the endoneurial space appeared denser in Δ10 mice (Fig. 6*D*). Electron microscopy showed that axon shape and myelination were globally normal (Fig. 6*E*). However, the diameter of the axons was significantly decreased (WT, 6.01 ± 0.08 μm, $n = 326$; Δ10, 5.68 ± 0.09 μm, $n = 294$; mean ± S.E., three mice/genotype, ~100 axons/animal; Mann-Whitney test, *, $p = 0.015$), and the myelin thickness was increased, as indicated by a significant reduction of the *g* ratio (WT, 0.792 ± 0.001, $n = 326$; Δ10, 0.754 ± 0.001, $n = 293$; mean ± S.E., three mice/genotype, ~100 fibers/animal; Mann-Whitney test, ***, $p < 0.001$). In register with the denser endoneurial space, collagen pockets between myelinated fibers were observed in Δ10 mice but not

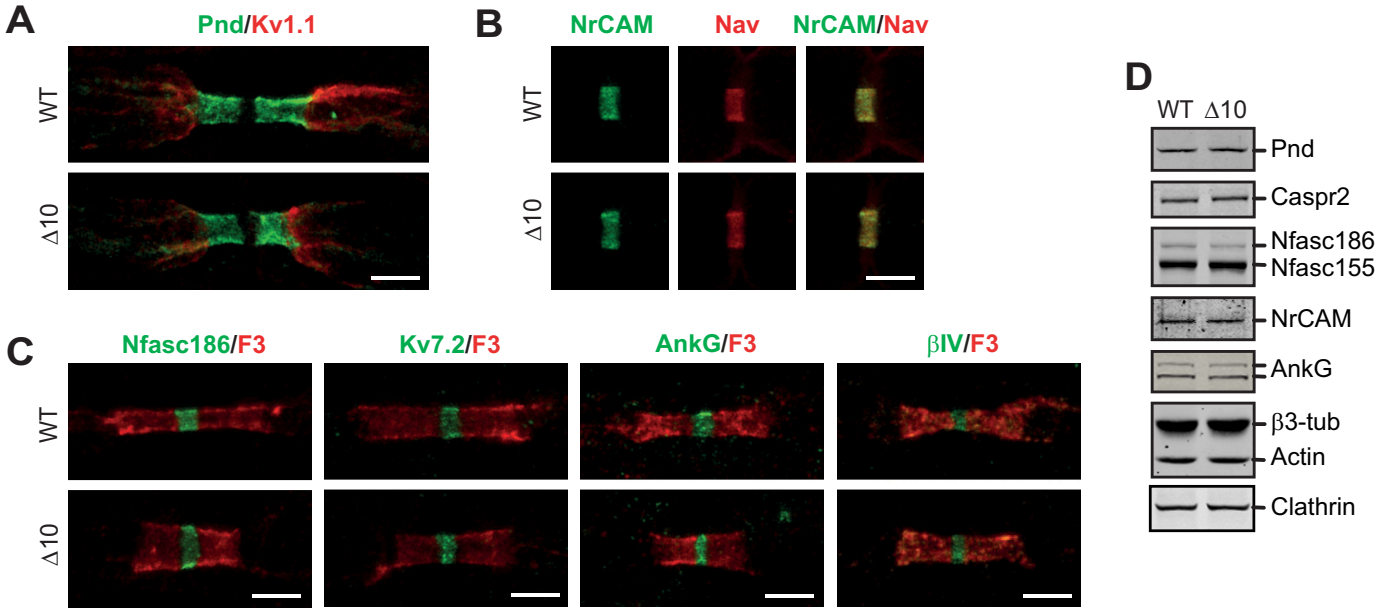

FIGURE 7. **Morphological alterations of PNS NR in Δ10 mice.** *A–C,* representative immunostaining of sciatic nerves fibers from 14-month-old WT and Δ10 mice for nodal, paranodal, and juxtaparanodal proteins (four mice/genotype). *A,* Caspr1/Pnd (*green*) and Kv1.1 (*red*). *B,* NrCAM (*green*) and Nav (*red*). *C,* Nfasc186, Kv7.2, AnkG, βIV-spectrin (βIV) (*green*) and contactin/F3 (F3) (*red*). *D,* protein expression in sciatic nerves from 8-month-old WT and Δ10 mice evaluated by immunoblotting. *Pnd*, Caspr1/paranodin; *Nfasc155/Nfasc186*, 155/186-kDa isoforms of neurofascin; *β3-tub*, neuronal β-tubulin. Clathrin was used to normalize protein expression. *Scale bars,* 5 μm.

in WT mice (Fig. 6*F*, *inset*). Furthermore, whereas in WT mice groups of unmyelinated fibers were regularly surrounded by a single Schwann cell process (Remak bundles) (Fig. 6*F*, *arrowheads*), in Δ10 mice Schwann cell processes often made several turns around small caliber axons (Fig. 6*F*, *arrowheads*). Altogether, these observations suggest that Δ10 mice present axonal loss with mild signs of neuropathy.

Morphological Alterations of PNS NR in Δ10 Mice—In peripheral nerves, NR are contacted by Schwann cell microvilli and flanked on either side by the paranodal and juxtaparanodal regions, which are defined by specific axoglial contacts and intercellular complexes (26, 27). To evaluate the importance of IQCJ-SCHIP1 in this organization over time, we examined the localization of nodal, paranodal, and juxtaparanodal molecular components in sciatic nerve fibers of young (2.5 months old) and older (14 months old) Δ10 mice. Immunolabeling for the paranodal proteins paranodin/Caspr1 (Pnd) and contactin/F3 (F3) appeared normal in Δ10 fibers at both ages (Fig. 7, *A* and *C*; 14-month-old mice). Immunolabeling for the juxtaparanodal Kv1.1 shaker-type channels were also similar in Δ10 and WT fibers (Fig. 7*A,* 14-month-old mice). In addition, there was no consistent difference in the distribution and clustering of the major membrane proteins of NR in the axolemma in mutant compared with WT mice, including Nav, NrCAM, Nfasc186, and Kv7.2, as well as the cytoskeletal proteins AnkG and βIV-spectrin (Fig. 7, *B* and *C,* 14-month-old mice). Accordingly, immunoblotting on sciatic nerve lysates of 8-month-old mice indicated that there were no significant alterations of the levels of major proteins of the paranodes (Pnd: WT, 100 ± 16%; Δ10, 103 ± 17%; mean ± S.E., $n = 3$ mice/genotype; *t* test, $t = 0.1229$, $p = 0.91$), juxtaparanodes (Caspr2: WT, 100 ± 18%; Δ10, 103 ± 7%; $t = 0.1704$, $p = 0.87$), and NR (Nfasc186: WT, 100 ± 31%; Δ10, 76 ± 17%; $t = 0.6696$, $p = 0.54$; NrCAM: WT, 100 ± 24%; Δ10, 92 ± 20%; $t = 0.2598$, $p = 0.81$; AnkG: WT, 100 ± 19%; Δ10, 112 ± 27%; $t = 0.354$, $p = 0.74$) (Fig. 7*D*). This indicates that IQCJ-SCHIP1 is not critical for nodal protein localization and enrichment. However, a detailed examination revealed a significant increase in the width (diameter) of NR, together with a significant decrease in their length in mutant mice as compared with WT mice (Fig. 7*C*; Table 2). These morphological abnormalities were observed in old mice (14 months old) as well as in younger mice (2.5 months old) (Table 2). They were associated with a significant reduction of the mean length/diameter ratio (Table 2). These observations suggest that IQCJ-SCHIP1 participates in the shape stabilization of NR.

Ultrastructural Alterations of PNS NR in Δ10 Mice—We further characterized the ultrastructure of NR by electron microscopy analysis on ultra-thin sections of sciatic and phrenic nerves. On longitudinal sections of sciatic nerves, the cytoplasmic glial loops contacting the axons at paranodes appeared globally normal in mutant mice (Fig. 8*A*). The transverse bands, the ultrastructural hallmark of paranodal junctions, were visible in mutant as well as in WT mice (Fig. 8*A*). Schwann cell microvilli filled the nodal gap and contacted the axon, and their organization was indistinguishable in mutant and WT mice (Fig. 8*B*). However, the presence of swollen and shorter NR was observed in Δ10 mice (Fig. 8*B*). In addition, the electron-dense coat beneath the nodal plasma membrane appeared scalloped (Fig. 8*B*). These observations indicate that IQCJ-SCHIP1 is required to stabilize the structural organization of NR and are consistent with morphological abnormalities detected by immunolabeling. Further analysis suggested an increased number of intra-axonal vesicles randomly distributed in the nodal regions of Δ10 mice as compared with WT mice (Fig. 8*B*, *arrows*). Quantification on ultra-thin transversal sections of phrenic nerves showed a significantly increased number of ves-

TABLE 2
Morphometric characteristics of sciatic nerve NR of WT and Δ10 mice
Measurements were performed on 100 NR/mice, four 14-month-old mice/genotypes, and three 2.5-month-old mice/genotype. Data are means ± S.E. Statistical analyses: Mann-Whitney *t* test, **, $p = 0.0036$; ***, $p < 0.0001$.

	NR diameter	NR length	Length/diameter ratio
	nm	*nm*	
14 months			
WT	2400 ± 32	1494 ± 10	0.662 ± 0.009
Δ10	2583 ± 39**	1431 ± 13***	0.596 ± 0.009***
2.5 months			
WT	2265 ± 27	1452 ± 11	0.669 ± 0.009
Δ10	2622 ± 38***	1377 ± 11***	0.559 ± 0.010***

icles (Fig. 8*C*, *arrows* and *arrowheads*), some with an electron-dense core (Fig. 8*C*, *arrows*), in the nodal region of mutant mice as compared with WT mice (WT, 8.048 ± 0.66 vesicles/section; Δ10, 13.31 ± 1.26 vesicles/section; mean ± S.E., $n = 42$ sections/genotype, three mice/genotype, 14 sections/animal; Mann-Whitney test, ***, $p = 0.0007$).

Moreover and interestingly, a detailed examination of the cytoskeleton in transverse sections revealed the presence of microtubules gatherings closely associated with mitochondria in nodal (Fig. 8*D*) and internodal regions (Fig. 8*E*) of mutant fibers. We quantified the number of microtubules localized 30 nm or closer to each mitochondria in the internodes. This number was significantly higher in Δ10 mice than in WT mice (WT, 5.04 ± 0.35; Δ10, 7.89 ± 0.43; Mann-Whitney test, $n = 48$ mitochondria/genotype, three mice/genotype, 16 mitochondria/animal, ***, $p < 0.0001$), indicating peri-mitochondrial spatial disorganization in mutant mice. This phenotype was independent from any obvious abnormalities in neurofilament density or organization (Fig. 8, *D*, and *E*) or significant change in the expression levels of the neurofilament subunits NF-H (WT, 100 ± 18%; Δ10, 113 ± 12%; mean ± S.E., $n = 3$ mice/genotype; *t* test, $t = 0.587$, $p = 0.59$), NF-M (WT, 100 ± 17%, Δ10, 106 ± 10%; $t = 0.315$, $p = 0.77$), and NF-L (WT, 100 ± 17%; Δ10, 113 ± 11%; $t = 0.638$, $p = 0.56$) (Fig. 8*F*). No change in neuronal tubulin (β3-tubulin) expression was detected in mutant mice (WT, 100 ± 7; Δ10, 107 ± 16; $n = 3$ mice/genotype; *t* test, $t = 0.417$, $p = 0.7$) (Fig. 8*F*). These observations suggest additional roles for SCHIP1 in axons, possibly in axonal transport.

Discussion

We previously characterized IQCJ-SCHIP1 as a partner of two cytoskeleton-associated proteins, schwannomin/merlin and the nodal protein AnkG. We identify here three additional nodal partners for IQCJ-SCHIP1, βIV-spectrin, Kv7.2, and Kv7.3 channels, and we show that IQCJ-SCHIP1 likely forms oligomers. These protein-protein interactions suggest that IQCJ-SCHIP1 could play multiple roles in the organization and/or function of NR by linking important proteins. Ultrastructural analyses revealed an altered shape of NR in mutant mice, indicating that IQCJ-SCHIP1 contributes to the nodal architecture. Nonetheless, IQCJ-SCHIP1 appears dispensable for nodal protein accumulation because the major nodal proteins are similarly enriched in young and old Δ10 mice.

IQCJ-SCHIP1 Associates with Multiple Nodal Proteins—Our previous work (15, 17) and this study demonstrate the ability of IQCJ-SCHIP1 to associate with multiple proteins of NR and therefore strongly support that IQCJ-SCHIP1 is a component of nodal complexes, which include channels, cell adhesion molecules, and the cytoskeletal proteins βIV-spectrin and AnkG. In peripheral myelinated fibers, ankyrin-spectrin complexes are not restricted to NR, and ankyrin-B (AnkB) and βII-spectrin are enriched at paranodes (28, 29). Importantly, we found that the interaction of IQCJ-SCHIP1 with βIV-spectrin requires the SD domain, which is absent in βII-spectrin or other β-spectrins (23). This provides a possible mechanism for the selective enrichment of IQCJ-SCHIP1 at AIS and NR where βIV-spectrin is localized. In addition, we previously showed that IQCJ-SCHIP1 interacts *in vitro* with the N-terminal ankyrin repeat domains of AnkG and AnkB with similar affinities, but these interactions require IQCJ-SCHIP1 phosphorylation by CK2, which is specifically concentrated in NR and also regulates AnkG interactions with βIV-spectrin, Nav, and Kv7 channels (17–20). Thus, multiple IQCJ-SCHIP1 protein-protein interactions as well as phosphorylation by CK2 appear to contribute to the highly specialized molecular organization of NR.

IQCJ-SCHIP1 Stabilizes Nodal Axon Membrane—We found that Δ10 mice present shorter and wider NR as compared with WT mice. These shape alterations were detectable in young as well as old mice, suggesting that IQCJ-SCHIP1 could contribute to nodal shape architecture. In mammalian cells, the mechanical support of the plasma membrane, as well as the microscale organization of membrane-spanning proteins, is provided by the association of spectrins and ankyrins, which promote the formation of an actin-based network coupled to the inner surface of the plasma membrane (30). Mutant mouse studies showed that βIVΣ6 plays a specific role in nodal Nav channel clustering, whereas βIVΣ1 stabilizes nodal membrane integrity (3, 4, 7). Mutant mice lacking βIVΣ1 present nodal shape alterations, which are very similar to those observed in Δ10 mice (3, 4). Some degree of nodal protrusion was also observed in qv_{3J} mice (5). This strongly suggests that IQCJ-SCHIP1 could contribute to the organization of the actin/βIV-spectrin/AnkG network to provide elastic and stable mechanical support of the plasma membrane.

Such a scaffolding role for IQCJ-SCHIP1 in cytoskeleton organization is supported by its ability to associate with both AnkG and βIV-spectrin. Moreover, we showed that the interactions with βIV-spectrin, AnkG, and Kv7 channels require N-terminal sequences of IQCJ-SCHIP1 but also its C-terminal region, which is likely to be implicated in its oligomerization (Fig. 9*A*). This raised the intriguing possibility that IQCJ-SCHIP1 could form complex oligomers through its C-terminal domain (see Fig. 4*C*) and expose its more N-terminal sequences to interact with its multiple partners, and thus contribute to organize protein networks. Protein flexibility and high surface charge have been found to be important properties for hub proteins, which interact with multiple proteins (31). Thus, the unfolded nature of IQCJ-SCHIP1 would fit well with a hub position in protein interaction networks.

The nanoscale architecture of AIS was recently resolved, showing that the actin/βIV-spectrin/AnkG submembranous cytoskeleton is organized as a periodic lattice of proteins that alternate between actin rings and βIV-spectrin·AnkG com-

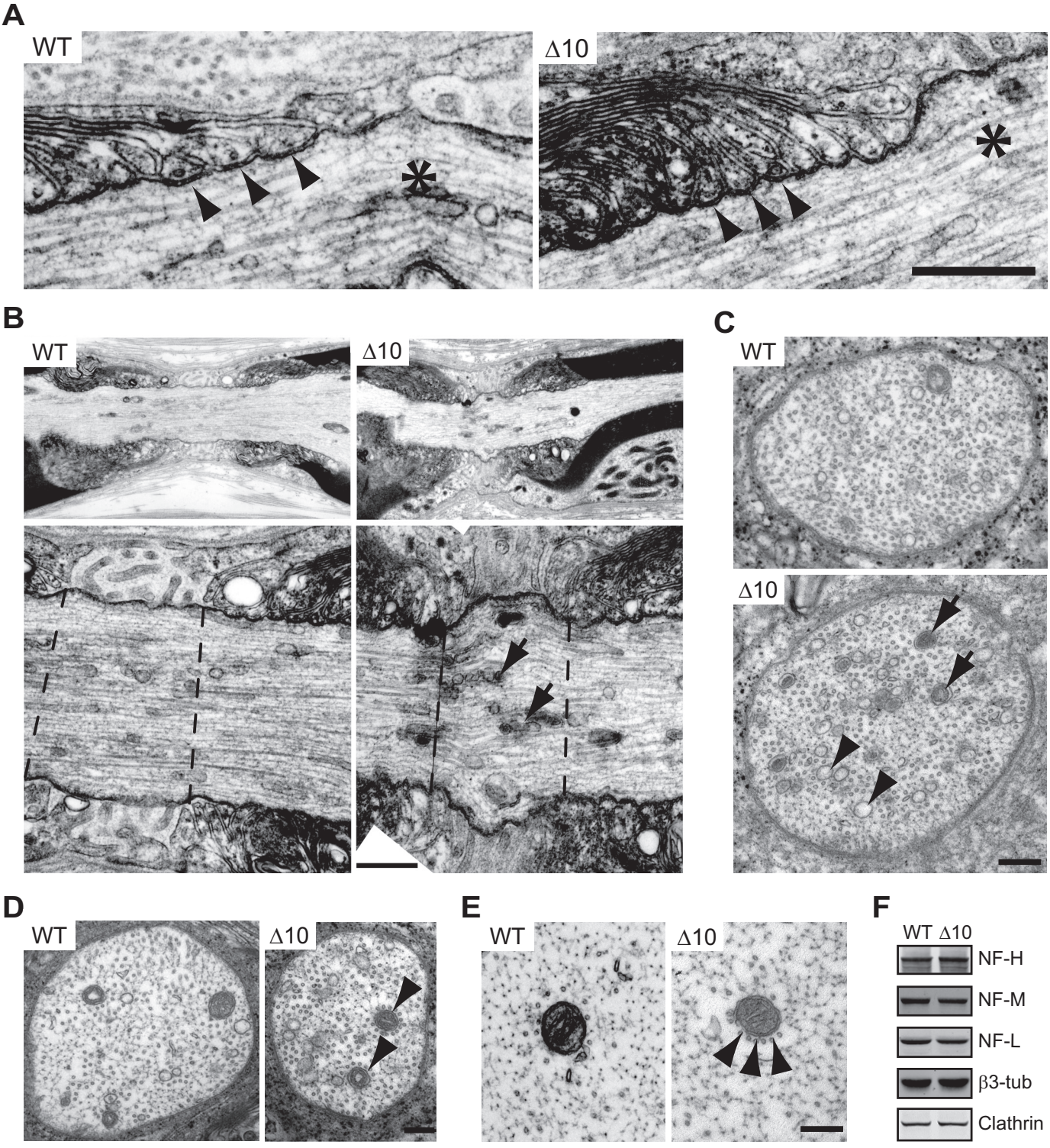

FIGURE 8. **Ultrastructural abnormalities of peripheral nerves in Δ10 mice.** *A* and *B,* representative electron micrographs of sciatic nerve longitudinal sections, at the level of NR, from 10-month-old mice WT and Δ10 mice (three mice/genotype). *A,* cytoplasmic glial loops contacting the axons at paranodes are globally normal in mutant mice, and the transverse bands (*arrowheads*) are visible in Δ10 mice as well as in WT mice. *Black asterisks* locate NR. *B,* Δ10 mice present swollen and shorter NR with an increased number of intra-axonal vesicles (*arrows*) as compared with WT mice. *Lower panels* correspond to high magnifications of *upper panels* at the level of NR. *Dashed lines* delineate NR. *C,* representative transversal sections of phrenic nerves at the level of NR showing that the axon of Δ10 mice contained a higher number of vesicles (*arrows, arrowheads*), some with an electron-dense core (*arrows*) (three mice/genotype). *D* and *E,* transversal sections of phrenic nerve at the level of NR (*D*) and the internode (*E*) showing that the axons of Δ10 mice present microtubules gatherings close to and surrounding mitochondria (*arrowheads*). *F,* expression of neurofilament subunits NF-H, NF-M, and LF-L, neuronal β-tubulin (*β3-tub*) and clathrin in sciatic nerves from 8-month-old WT and Δ10 mice evaluated by immunoblotting. Protein lysates were the same as those used to quantify the expression levels of the proteins of the nodes of Ranvier. Immunoblots for β-tubulin and clathrin are consequently identical to those presented in Fig. 7*D*. Clathrin was similarly used to normalize protein expression. *Scale bars, A* and *B*, 0.5 μm; *C* and *D*, 200 nm; *E,* 100 nm.

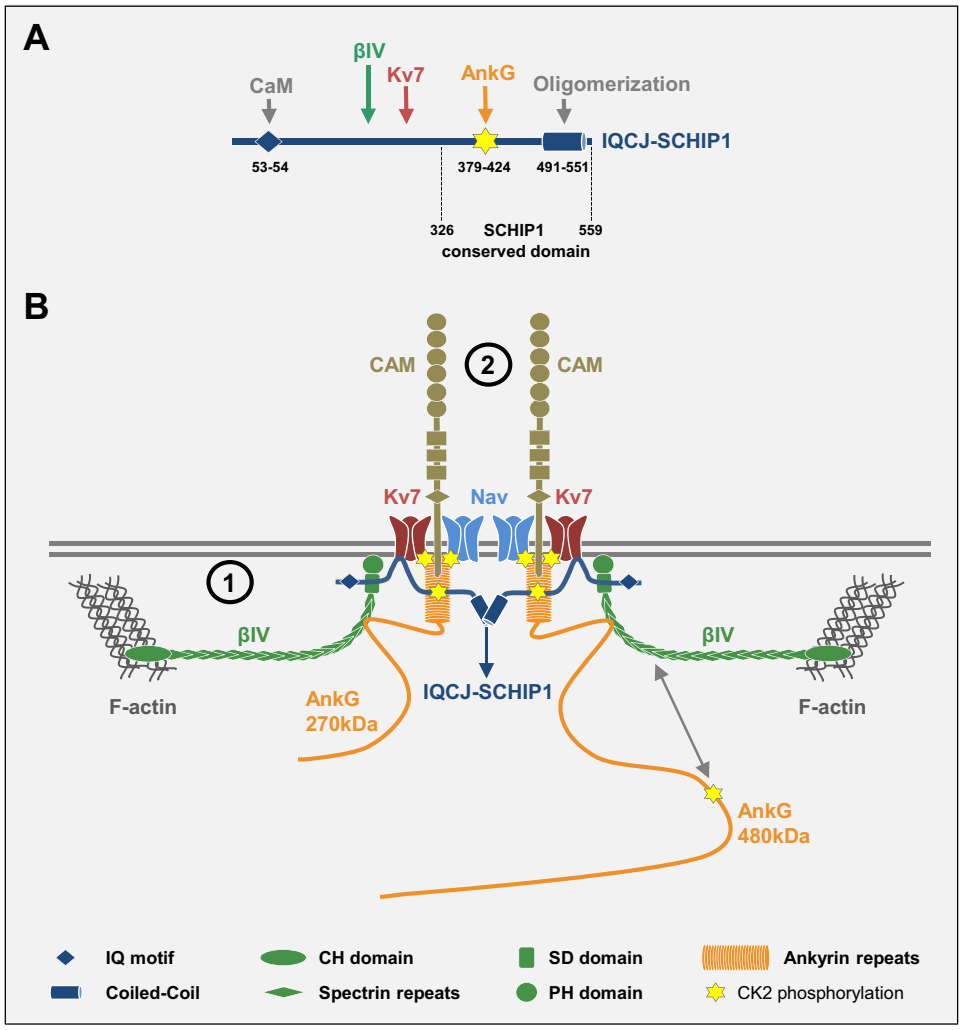

FIGURE 9. *A,* schematic structure and interacting partners of IQCJ-SCHIP1. IQCJ-SCHIP1 is able to oligomerize through its C-terminal coiled-coil region and to interact with AnkG, βIV-spectrin, and Kv7 through more N-terminal sequences. Its interaction with AnkG requires its phosphorylation by CK2. *Numbers* correspond to amino acid residues. *Dashed lines* delineate the C-terminal domain, which is conserved in the six isoforms of SCHIP1 and found in almost all animals (annotated in Pfam as "SCHIP-1 domain," PF10148). *B,* schematic model of IQCJ-SCHIP1-containing molecular complexes at NR. IQCJ-SCHIP1 interacts with the intracellular C-terminal domain of Kv7 channels, the SD domain of βIV-spectrin, and the membrane-binding domain of AnkG (270/480 kDa), which by itself associates with Nav/Kv7 channels, cell adhesion molecules (*CAM*), and βIV-spectrin. The submembrane cytoskeleton is organized as a periodic lattice that alternates between F-actin rings and βIV-spectrin·AnkG complexes. Longitudinal head-to-tail βIV-spectrin subunits connect F-actin rings at their N-terminal extremities to AnkG·channels·CAM complexes near their SD domains. Through oligomerization, IQCJ-SCHIP1 could indirectly link βIV-spectrin subunits in a head-to-tail manner (*1*) and contribute to Nav/Kv7 channels and CAM microscale organization within membrane complexes by controlling the AnkG/βIV-spectrin network organization (*2*).

plexes (32–35). NR appear to present a similar architecture (33, 34). The periodic cytoskeleton lattice was also observed in distal axons, where actin rings alternate with βII-spectrin (32–34). In that case, actin rings were proposed to be connected by typical head-to-tail βII-spectrin/α-spectrin tetramers. At AIS, the periodicity of the lattice was shown to result from longitudinal head-to-tail βIV-spectrin subunits connecting actin rings at their N-terminal extremities to AnkG·Nav channel complexes near their C-terminal SD domains (Fig. 9*B*) (35). However, no α-spectrin subunit has been reported in AIS or in NR. Because IQCJ-SCHIP1 interacts with the C-terminal βIV-spectrin SD domain, we propose that, through its oligomerization, IQCJ-SCHIP1 could serve to indirectly link βIV-spectrin molecules in a head-to-tail manner (Fig. 9*B*). This hypothesis implies that βIV-spectrin and IQCJ-SCHIP1 mutations would somehow lead to similar cytoskeleton disturbance. Thus, it is consistent with the fact Δ10 and βIV-spectrin mutant mice present similar nodal shape alterations (Refs. 3–5 and this study).

The persistence of NrCAM, Nfasc186, and Nav and Kv7 channels in NR of Δ10 mutant mice indicates that the interactions of IQCJ-SCHIP1 with βIV-spectrin and/or AnkG are not strictly required for nodal membrane protein clustering. However, because most of these membrane proteins are able to interact with AnkG, we suggest that IQCJ-SCHIP1 could contribute to their microscale organization within membrane complexes by controlling the AnkG/βIV-spectrin network organization (Fig. 9*B*). The ability of IQCJ-SCHIP1 to associate with Kv7 channels could also serve this function for Kv7 channels by connecting them indirectly with βIV-spectrin.

Remarkably, we showed that the N-terminal IQCJ domain of IQCJ-SCHIP1 is not required for its interactions with βIV-spectrin, AnkG, and Kv7 channels (Fig. 3, *F* and *G*) (17). This

questions whether this domain could mediate the association of IQCJ-SCHIP1 with additional non-identified nodal partners and/or whether it could contribute to regulate *in vivo* complex formations through its ability to interact with CaM in the absence of calcium. Of interest, Leterrier *et al.* (35) showed that an acute intracellular calcium increase has a strong effect on the periodicity of the AIS submembrane lattice.

Additional Axonal and/or Glial Roles for SCHIP1?—NR are sites of vesicle membrane compartment accumulation, which results from local transport retardation and is thought to serve nodal membrane processing and/or turnover (36). A finding of our study is that Δ10 mice present an increase number of nodal vesicles, which interestingly, was also observed in βIVΣ1 and qv_{3J} mutant mice (3, 5) and could therefore result from abnormal nodal membrane processing and/or stability. Electron microscopy showed in addition an abnormal spatial organization of microtubules around mitochondria at NR and all along the axon. The functional relevance of this phenotype is not known because to our knowledge it was not described before. Interestingly, the coiled-coil region of SCHIP1 presents sequence homologies with a coiled-coil region within the C-terminal domain of the protein FEZ1 (8), which plays a role in kinesin-mediated anterograde transport of vesicles and mitochondria in axons (37–39). In addition, although we showed that the SD domain of βIV-spectrin is the primary binding site for SCHIP1, our results do not strictly exclude the possibility that SCHIP1 could interact with other β-spectrins such as βIII-spectrin, which has been shown to interact with dynactin (40) and is implicated in dynein-mediated vesicular transport (41, 42). This raises the intriguing hypothesis that SCHIP1 could play a role in anterograde and/or retrograde microtubule-based axonal transport. Axonal trafficking defects could thus contribute to vesicle accumulation at nodes in Δ10 mice and possibly to the wrinkled aspect of the nodal membrane as a result of defects in the balance of membrane delivery/recovery. A role for SCHIP1 in axonal transport would also be consistent with the axonal loss observed in mutant mice.

Structural analyses also revealed an axon diameter decrease and a myelin thickness increase in Δ10 mice. The mechanisms underlying this phenotype may be complex because the development of unmyelinated and myelinated fibers depends on communication between axons and Schwann cells, and both myelin and axon defects may therefore be of glial and/or axonal origin. However, schwannomin knockdown in either neurons or Schwann cells also results in hypermyelination in mice (43, 44), thus raising the possibility that SCHIP1 could contribute to glial and/or neuronal functions of schwannomin in myelination.

In conclusion, we provide here evidence for the importance of SCHIP1 in the organization of peripheral myelinated fibers. We show that through its ability to interact with several nodal partners, IQCJ-SCHIP1 appears to be important for the organization of molecular complexes of peripheral NR. Through its oligomerization and multiple interactions, IQCJ-SCHIP1 may contribute to the high scale organization of the actin/AnkG/βIV-spectrin network, thus providing elastic and stable mechanical support of the nodal plasma membrane.

Experimental Procedures

Antibodies

Rabbit antibodies directed against Kv7.2, Caspr2, neurofascin, and Pnd (L51) and chicken SCHIP1 antibody 959 were previously described (8, 15, 16, 43, 45–47). The rabbit antibody directed against the SD domain of βIV-spectrin and the rabbit antibody directed against AnkG were generous gifts from Dr. Michele Solimena and Dr. Ekaterini Kordeli, respectively. Commercial primary antibodies were from the following sources: Nav α-subunit, mouse clone K58/35 catalogue no. S8809, Sigma; $K_v1.1$ α subunit, mouse clone K20/78 catalogue no. 75-007, NeuroMab; F3, goat catalogue no. AF904, R&D Systems; NrCAM, rabbit catalogue no. ab24344, Abcam; Nfasc186, rabbit catalogue no. ab31719, Abcam; FLAG, rabbit catalogue no. F7425 or mouse clone M2 catalogue no. F1804, Sigma; Myc, rabbit catalogue no. 2272 or mouse clone 9B11 catalogue no. 2276, Cell Signaling; HA, rat clone 3F10 catalogue no. 11 867 423 001, Roche Applied Science; V5, rabbit catalogue no. AB3792, Merck-Millipore; GFP, rabbit catalogue no. A6455, Thermo Fisher Scientific; neuronal class III β-tubulin, mouse clone TUJ1 catalogue no. MMS-435P, Covance; actin, mouse clone C4 catalogue no. MAB1501, Merck-Millipore; clathrin heavy chain, rabbit catalogue no. ab21679, Abcam. Secondary antibodies for immunohistochemistry (Alexa Fluor 488-, 546-, or 633-conjugated) were from Thermo Fisher Scientific. Secondary antibodies for immunoblotting (IRDye™800CW or IRDye™700CW) were from Rockland Immunochemicals.

Plasmid Constructs

The expression vectors for the Myc-tagged Σ6 isoform of βIV-spectrin (mouse cDNA, accession number AB055621), HA-tagged βIV-spectrin C-terminal part (human cDNA, accession number AF082075), and GFP-tagged βII-spectrin (human cDNA, accession number NM_003128) were generous gifts from Dr. Masayuki Komada (7), Dr. Michele Solimena (23), and Dr. Vann Bennett (48), respectively. The expression vectors for V5-tagged Kv7.3 (rat cDNA, accession number AF091247) and V5-tagged WT or mutant Kv7.2 (Kv7.2-L586P, Kv7.2-L638P, Kv7.2-I340A, and Kv7.2-Δ535–557) (mouse cDNA, accession number AF490773) were previously described (49). The expression vectors for the GFP-tagged βIV-spectrin C-terminal parts were obtained by mouse cDNA amplification and subcloning in the pEGFP-C1 vector (Clontech). Vectors expressing other Kv7.2 and βIV-spectrin variants were similarly obtained by cDNA amplification and subcloning. For the expression vectors for HA-tagged IQCJ-SCHIP1, FLAG-tagged SCHIP1a, and FLAG-tagged WT or mutant IQCJ-SCHIP1, the mouse cDNAs of IQCJ-SCHIP1 (accession number EU163409) or SCHIP1a (accession number EU163407) were cloned by PCR into the pCB6-HA vector previously described (8) or into the pFLAG-CMV-2 vector (Sigma), respectively.

Cell Cultures, Co-immunoprecipitations, and Immunoblottings

COS-7 cells were transfected using ExGen 500 according to the manufacturer's recommendations (Euromedex) using 10 μg of plasmid/2×10^6 cells/100-mm dish and were grown 24 h before processing. Co-immunoprecipitations were performed

essentially as described previously (50). For SCHIP1/βIV-spectrin and SCHIP1/βII-spectrin co-immunoprecipitations, the extraction buffer and the washing buffer contained 50 mM Tris, pH 7.6, 150 mM NaCl, 1 mM EDTA, Complete protease inhibitors (Roche Applied Science), and 1 or 0.5% Triton X-100 (v/v), respectively. For SCHIP1/Kv7 co-immunoprecipitations and SCHIP1 oligomerization studies, the extraction buffer and the washing buffer contained 10 mM Tris, pH 7.4, 100 mM KCl, Complete protease inhibitors, and 1 or 0.5% Triton X-100, respectively. Precipitated proteins were separated by electrophoresis in NuPAGE 8–12% BisTris gels or NuPAGE 3–8% Tris acetate gels (Thermo Fisher Scientific) and transferred to 0.45-μm nitrocellulose membrane in 25 mM Tris-HCl, pH 7.4, 192 mM glycine, and 20% ethanol. Membranes were blocked with 5% nonfat dry milk in TBS/Tween 0.1% (v/v, TBST) 1 h at room temperature, incubated with primary antibodies in the same buffer for 2 h and then 1 h with appropriate IRDye-conjugated secondary antibodies, and imaged using Odyssey Imaging System (LI-COR Biosciences). For oligomerization analysis, cell lysates were prepared in the extraction buffer used for SCHIP1/Kv7 co-immunoprecipitations, and proteins were separated on Native PAGE 3–8% BisTris gels (Thermo Fisher Scientific).

Schip1 Mutant Mice

*Schip1*Δ10 mice were previously described (16). Animal research was conducted according to the French and European guidelines (EC directive 86/609, French MESR 00984.01). Animal experimentations were approved by the Direction Départementale des Services Vétérinaires de Paris, Service de la Protection et de la Santé Animales et de la Protection de l'Environnement (license B75-05-22). The principal investigator had a personal authorization (L Goutebroze, license 75-1533).

Behavioral Tests

The behavioral phenotype of WT and Δ10 littermate mice (4–6 months old) was examined during footprinting, grid, grip, and hot plate tests. All tests were performed in sound-attenuated rooms, between 9 a.m. and 5 p.m. Mice were group-housed with *ad libitum* access to food and water and a 12–12 h light-dark cycle (light phase onset at 7 a.m.). For most experiments and initial quantitative analyses, the experimenter was blinded to the genotype of the mice tested and analyzed.

Footprint Pattern Analysis—The gait analysis method was modified from Refs. 51, 52. Mice (three of each genotype) were tested in a confined walkway 4.5 cm wide and 100 cm long with 10-cm high walls and a dark shelter at the end. Mice were trained several times to walk into the dark compartment. The footprints were obtained by dipping the hind paws into ink, before they walked down the corridor on white paper. The footprint patterns generated were scored for angles with regard to walking direction (ImageJ software, NCBI).

Grid Test—Coordination between forelimbs and hind limbs and accurate limb placement were examined by assessing the ability to walk on metal grid bars with 1.5-cm gaps on the bottom of a 30 × 20 × 20-cm box. The performance of each animal (six of each genotype) was analyzed by counting the number of errors in foot placement/total number of steps, during the 2-min sessions, once a day, for 3 consecutive days. On the day prior to data collection, each mouse was allowed to walk on the grid for 2 min.

Wire-hanging Test—The wire-hanging test was performed to measure neuromuscular strength. Mice (6–9/genotype) were gently placed on a wire-cage lid, which was then slowly waved and turned upside down above the soft bedding. The hanging time for each mouse to fall onto the bedding below was measured with a cutoff time of 60 s.

Grip Strength Analysis—Forelimb grip strength was measured using a Grip Strength Meter (Bioseb). Mice (7–9/genotype) were held by the tail and allowed to grasp a trapeze bar with their forepaws. Once the mouse grasped the bar with both paws, the mouse was pulled away from the bar until the mouse released the bar. The digital meter displays the level of tension (in grams) exerted on the bar by the mouse.

Hot Plate—A standard hot plate (Bioseb), adjusted to 52 °C, was used to assess motor reactions in response to noxious stimuli. Mice (7–9/genotype) were confined on the plate by a Plexiglas cylinder (diameter 19 cm, height 26 cm). The latency to a hind paw response (licking or shaking) or jumping, whatever happened first, was taken as the nociceptive threshold.

Immunohistochemistry and Image Analysis

Sciatic nerves of mice (2.5 months old, three of each genotype; 14 months old, four of each genotype) were dissected and fixed in 2% paraformaldehyde for 30 min at room temperature, teased apart to yield single fiber preparations, air-dried, and kept at −20 °C. Immunofluorescent staining was performed as described previously (53). Briefly, slides were treated with 0.1 M glycine for 30 min, preincubated for 1 h at room temperature in 2 g/liter porcine skin gelatin and 2.5 ml/liter Triton X-100 in PBS (PGT buffer), before incubation with primary antibodies (diluted in PGT) overnight at 4 °C. After washing with PBS, coverslips were incubated for 2 h at room temperature with secondary antibodies (diluted in PGT), washed again with PBS, and mounted in Vectashield. Images were acquired using a Leica SP5 confocal laser-scanning microscope (Leica Microsystems). Measurements of NR width (perpendicular to the axon axis) and length (parallel to the axon axis) were performed on images of NrCAM labeling acquired with a DM6000-2 Leica microscope equipped with a CCD camera, using ImageJ software (100 NR/animal).

Electron Microscopy and Morphometry

Mice (10 months old, three of each genotype) were anesthetized with pentobarbital and perfused with 9 g/liter NaCl, followed by 40 g/liter paraformaldehyde and 30 g/liter glutaraldehyde in 0.1 M phosphate buffer (PB). The sciatic and phrenic nerves were removed and placed in fresh fixative overnight at 4 °C, rinsed in PB, post-fixed in 20 g/liter OsO_4 in PB, dehydrated in an ascending series of ethanol, and embedded in epoxy resin. Morphometric analyses were performed on 0.5-μm-thick semi-thin transversal sections of phrenic nerves stained with toluidine blue and visualized with a DM6000 Leica microscope. Fibers and axon diameters, and *g* ratios, defined as ratios of axonal to fiber's diameter, were measured with

DigitalMicrograph software (Gatan), for ~100 fibers/animal. Ultrastructural studies were performed on phrenic nerve transversal sections and sciatic nerve longitudinal sections. Ultrathin sections (40 nm) were stained with Reynold's lead citrate and uranyl acetate and examined with a Philipps CM-100 transmission electron microscope. Images were acquired using an Orius (Gatan) digital camera. Ten NR were examined in longitudinal sections of sciatic nerves from mice of each genotype. Quantification of the number of vesicles per NR section (14 sections/animal) and the distance between microtubules and mitochondria in the internodes (17 mitochondria/animal) was performed on phrenic nerve transversal sections using the DigitalMicrograph software (Gatan).

Sciatic Nerve Lysate Preparation and Immunoblotting

Sciatic nerves of mice (8 months old, three of each genotype) were dissected out and homogenized in a Dounce vessel containing 200 μl of a lysis buffer containing 10 mM NaP_i buffer, pH 7.8, 59 mM NaCl, 1 ml/liter Triton X-100 g/liter deoxycholate, 1 g/liter SDS, 100 ml/liter glycerol, 25 mM β-glycerophosphate, 50 mM NaF, 2 mM Na_3VO_4, and Complete protease inhibitors. Homogenates were centrifuged for 30 min at 4 °C at 20,000 $\times$ *g*, and protein concentration in the supernatants was determined by the bicinchoninic acid method (Sigma). Equal amounts of protein (40 μg) were loaded in NuPAGE 8–12% BisTris gels (Thermo Fisher Scientific), and immunoblots were performed as described above. The expression levels of the proteins were quantified using Odyssey Imaging System (LI-COR Biosciences) and normalized on clathrin expression, which was not expected to be affected in Δ10 mice.

Electrophysiological Analysis

Mice (8 months old, 4–5/genotype) were euthanized, and the sciatic nerves were quickly dissected out and transferred into artificial cerebrospinal fluid containing 126 mM NaCl, 3 mM KCl, 2 mM $CaCl_2$, 2 mM $MgSO_4$, 1.25 NaH_2PO_4, 26 mM $NaHCO_3$, and 10 mM dextrose, pH 7.4–7.5. The sciatic nerves (2-cm segments) were placed in a three-compartment recording chamber and perfused at 1–2 ml/min in medium equilibrated with 95% O_2 and 5% CO_2. The distal end was stimulated supramaximally (40-μs duration) through two electrodes isolated with petroleum jelly, and recordings were performed at the proximal ends. Signals were amplified and digitized at 500 kHz. The duration of the CAPs was calculated at the half-maximal amplitude ($V_{½}$). The delay of the CAPs was measured at $V_{½}$ and at the maximal amplitude (V_{max}). The conduction velocity was derived from the delay. For recruitment analysis, the CAP amplitude was measured and plotted as a function of the stimulation intensity. For the refractory period analysis, two successive stimuli were applied at different intervals, and the amplitude of the second CAP was measured and plotted as a function of the delay between the two stimuli.

Bioinformatics and Statistical Analysis

Secondary structure and oligomerization were predicted using the FoldIndex and MULTICOILS software, respectively. Statistical analyses were performed with GraphPad Prism 5 software. For variables that did not follow a normal distribution, statistical analyses were carried out using the Mann-Whitney rank sum test to compare quantitative variables between WT and Δ10 mice. Significant main effects were further analyzed by post hoc comparisons of means using *t* tests. The significance was established at a p value <0.05.

Author Contributions—P.-M. M., J. D., and L. G. designed the research; P.-M. M., C. C.-D., J. D., M. G, J. B., S. T., E. K., and L. G. performed the research; P.-M. M., C. C. D., M. G., J. D., J.-A. G., and L. G. analyzed the data; and J. D., J.-A. G., and L. G. wrote the paper.

Acknowledgments—Equipment at the Institut du Fer à Moulin was supported in part by DIM NeRF from Région Ile-de-France (NERF, 10016908) and by the Fondation pour la Recherche Médicale/Rotary "Espoir en tête." We are grateful to R. Boukhari, N. Roblot, Y. Bertelle, A. Rousseau, M. Savariradjane, and T. Eirinopoulou (Institut du Fer à Moulin Cell and Tissue Imaging facility) for animal care and assistance with microscopes. The teams of J.-A.G. and L. G. are affiliated with the Paris School of Neuroscience (ENP) and the Bio-Psy laboratory of excellence.

References

1. Zollinger, D. R., Baalman, K. L., and Rasband, M. N. (2015) The ins and outs of polarized axonal domains. *Annu. Rev. Cell Dev. Biol.* **31,** 647–667
2. Zhang, C., and Rasband, M. N. (2016) Cytoskeletal control of axon domain assembly and function. *Curr. Opin. Neurobiol.* **39,** 116–121
3. Lacas-Gervais, S., Guo, J., Strenzke, N., Scarfone, E., Kolpe, M., Jahkel, M., De Camilli, P., Moser, T., Rasband, M. N., and Solimena, M. (2004) βIVΣ1 spectrin stabilizes the nodes of Ranvier and axon initial segments. *J. Cell Biol.* **166,** 983–990
4. Uemoto, Y., Suzuki, S., Terada, N., Ohno, N., Ohno, S., Yamanaka, S., and Komada, M. (2007) Specific role of the truncated βIV-spectrin Σ6 in sodium channel clustering at axon initial segments and nodes of Ranvier. *J. Biol. Chem.* **282,** 6548–6555
5. Yang, Y., Lacas-Gervais, S., Morest, D. K., Solimena, M., and Rasband, M. N. (2004) βIV spectrins are essential for membrane stability and the molecular organization of nodes of Ranvier. *J. Neurosci.* **24,** 7230–7240
6. Ho, T. S., Zollinger, D. R., Chang, K. J., Xu, M., Cooper, E. C., Stankewich, M. C., Bennett, V., and Rasband, M. N. (2014) A hierarchy of ankyrin-spectrin complexes clusters sodium channels at nodes of Ranvier. *Nat. Neurosci.* **17,** 1664–1672
7. Komada, M., and Soriano, P. (2002) βIV-spectrin regulates sodium channel clustering through ankyrin-G at axon initial segments and nodes of Ranvier. *J. Cell Biol.* **156,** 337–348
8. Goutebroze, L., Brault, E., Muchardt, C., Camonis, J., and Thomas, G. (2000) Cloning and characterization of SCHIP-1, a novel protein interacting specifically with spliced isoforms and naturally occurring mutant NF2 proteins. *Mol. Cell. Biol.* **20,** 1699–1712
9. Perisic, L., Rodriguez, P. Q., Hultenby, K., Sun, Y., Lal, M., Betsholtz, C., Uhlén, M., Wernerson, A., Hedin, U., Pikkarainen, T., Tryggvason, K., and Patrakka, J. (2015) Schip1 is a novel podocyte foot process protein that mediates actin cytoskeleton rearrangements and forms a complex with Nherf2 and ezrin. *PLoS ONE* **10,** e0122067
10. Auranen, M., Varilo, T., Alen, R., Vanhala, R., Ayers, K., Kempas, E., Ylisaukko-Oja, T., Peltonen, L., and Järvelä, I. (2003) Evidence for allelic association on chromosome 3q25–27 in families with autism spectrum disorders originating from a subisolate of Finland. *Mol. Psychiatry* **8,** 879–884
11. Coon, H., Matsunami, N., Stevens, J., Miller, J., Pingree, C., Camp, N. J., Thomas, A., Krasny, L., Lainhart, J., Leppert, M. F., and McMahon, W. (2005) Evidence for linkage on chromosome 3q25–27 in a large autism extended pedigree. *Hum. Hered.* **60,** 220–226
12. Hu, V. W., Frank, B. C., Heine, S., Lee, N. H., and Quackenbush, J. (2006) Gene expression profiling of lymphoblastoid cell lines from monozygotic twins discordant in severity of autism reveals differential regulation of neurologically relevant genes. *BMC Genomics* **7,** 118

13. Kwaśnicka-Crawford, D. A., Carson, A. R., and Scherer, S. W. (2006) IQCJ-SCHIP1, a novel fusion transcript encoding a calmodulin-binding IQ motif protein. *Biochem. Biophys. Res. Commun.* **350,** 890–899
14. Chung, H. L., Augustine, G. J., and Choi, K. W. (2016) *Drosophila* schip1 links expanded and Tao-1 to regulate hippo signaling. *Dev. Cell* **36,** 511–524
15. Martin, P. M., Carnaud, M., Garcia del Caño, G., Irondelle, M., Irinopoulou, T., Girault, J. A., Dargent, B., and Goutebroze, L. (2008) Schwannomin-interacting protein-1 isoform IQCJ-SCHIP-1 is a late component of nodes of Ranvier and axon initial segments. *J. Neurosci.* **28,** 6111–6117
16. Klingler, E., Martin, P. M., Garcia, M., Moreau-Fauvarque, C., Falk, J., Chareyre, F., Giovannini, M., Chédotal, A., Girault, J. A., and Goutebroze, L. (2015) The cytoskeleton-associated protein SCHIP1 is involved in axon guidance, and is required for piriform cortex and anterior commissure development. *Development* **142,** 2026–2036
17. Papandréou, M. J., Vacher, H., Fache, M. P., Klingler, E., Rueda-Boroni, F., Ferracci, G., Debarnot, C., Pipéroglou, C., Garcia Del Caño, G., Goutebroze, L., and Dargent, B. (2015) CK2-regulated schwannomin-interacting protein IQCJ-SCHIP-1 association with AnkG contributes to the maintenance of the axon initial segment. *J. Neurochem.* **134,** 527–537
18. Jenkins, P. M., Kim, N., Jones, S. L., Tseng, W. C., Svitkina, T. M., Yin, H. H., and Bennett, V. (2015) Giant ankyrin-G: a critical innovation in vertebrate evolution of fast and integrated neuronal signaling. *Proc. Natl. Acad. Sci. U.S.A.* **112,** 957–964
19. Bréchet, A., Fache, M. P., Brachet, A., Ferracci, G., Baude, A., Irondelle, M., Pereira, S., Leterrier, C., and Dargent, B. (2008) Protein kinase CK2 contributes to the organization of sodium channels in axonal membranes by regulating their interactions with ankyrin G. *J. Cell Biol.* **183,** 1101–1114
20. Xu, M., and Cooper, E. C. (2015) An ankyrin-G N-terminal gate and protein kinase CK2 dually regulate binding of voltage-gated sodium and KCNQ2/3 potassium channels. *J. Biol. Chem.* **290,** 16619–16632
21. Parkinson, N. J., Olsson, C. L., Hallows, J. L., McKee-Johnson, J., Keogh, B. P., Noben-Trauth, K., Kujawa, S. G., and Tempel, B. L. (2001) Mutant β-spectrin 4 causes auditory and motor neuropathies in quivering mice. *Nat. Genet.* **29,** 61–65
22. Devaux, J. J. (2010) The C-terminal domain of ssIV-spectrin is crucial for KCNQ2 aggregation and excitability at nodes of Ranvier. *J. Physiol.* **588,** 4719–4730
23. Berghs, S., Aggujaro, D., Dirkx, R., Jr, Maksimova, E., Stabach, P., Hermel, J. M., Zhang, J. P., Philbrick, W., Slepnev, V., Ort, T., and Solimena, M. (2000) βIV spectrin, a new spectrin localized at axon initial segments and nodes of Ranvier in the central and peripheral nervous system. *J. Cell Biol.* **151,** 985–1002
24. Tse, W. T., Tang, J., Jin, O., Korsgren, C., John, K. M., Kung, A. L., Gwynn, B., Peters, L. L., and Lux, S. E. (2001) A new spectrin, βIV, has a major truncated isoform that associates with promyelocytic leukemia protein nuclear bodies and the nuclear matrix. *J. Biol. Chem.* **276,** 23974–23985
25. Haitin, Y., and Attali, B. (2008) The C-terminus of Kv7 channels: a multifunctional module. *J. Physiol.* **586,** 1803–1810
26. Salzer, J. L., Brophy, P. J., and Peles, E. (2008) Molecular domains of myelinated axons in the peripheral nervous system. *Glia* **56,** 1532–1540
27. Buttermore, E. D., Thaxton, C. L., and Bhat, M. A. (2013) Organization and maintenance of molecular domains in myelinated axons. *J. Neurosci. Res.* **91,** 603–622
28. Cifuentes-Diaz, C., Chareyre, F., Garcia, M., Devaux, J., Carnaud, M., Levasseur, G., Niwa-Kawakita, M., Harroch, S., Girault, J. A., Giovannini, M., and Goutebroze, L. (2011) Protein 4.1B contributes to the organization of peripheral myelinated axons. *PLoS ONE* **6,** e25043
29. Ogawa, Y., Schafer, D. P., Horresh, I., Bar, V., Hales, K., Yang, Y., Susuki, K., Peles, E., Stankewich, M. C., and Rasband, M. N. (2006) Spectrins and ankyrinB constitute a specialized paranodal cytoskeleton. *J. Neurosci.* **26,** 5230–5239
30. Bennett, V., and Lorenzo, D. N. (2013) Spectrin- and ankyrin-based membrane domains and the evolution of vertebrates. *Curr. Top. Membr.* **72,** 1–37
31. Patil, A., and Nakamura, H. (2006) Disordered domains and high surface charge confer hubs with the ability to interact with multiple proteins in interaction networks. *FEBS Lett.* **580,** 2041–2045
32. Xu, K., Zhong, G., and Zhuang, X. (2013) Actin, spectrin, and associated proteins form a periodic cytoskeletal structure in axons. *Science* **339,** 452–456
33. D'Este, E., Kamin, D., Göttfert, F., El-Hady, A., and Hell, S. W. (2015) STED nanoscopy reveals the ubiquity of subcortical cytoskeleton periodicity in living neurons. *Cell Rep.* **10,** 1246–1251
34. D'Este, E., Kamin, D., Velte, C., Göttfert, F., Simons, M., and Hell, S. W. (2016) Subcortical cytoskeleton periodicity throughout the nervous system. *Sci. Rep.* **6,** 22741
35. Leterrier, C., Potier, J., Caillol, G., Debarnot, C., Rueda Boroni, F., and Dargent, B. (2015) Nanoscale architecture of the axon initial segment reveals an organized and robust scaffold. *Cell Rep.* **13,** 2781–2793
36. Zimmermann, H. (1996) Accumulation of synaptic vesicle proteins and cytoskeletal specializations at the peripheral node of Ranvier. *Microsc. Res. Tech.* **34,** 462–473
37. Fujita, T., Maturana, A. D., Ikuta, J., Hamada, J., Walchli, S., Suzuki, T., Sawa, H., Wooten, M. W., Okajima, T., Tatematsu, K., Tanizawa, K., and Kuroda, S. (2007) Axonal guidance protein FEZ1 associates with tubulin and kinesin motor protein to transport mitochondria in neurites of NGF-stimulated PC12 cells. *Biochem. Biophys. Res. Commun.* **361,** 605–610
38. Ikuta, J., Maturana, A., Fujita, T., Okajima, T., Tatematsu, K., Tanizawa, K., and Kuroda, S. (2007) Fasciculation and elongation protein ζ-1 (FEZ1) participates in the polarization of hippocampal neuron by controlling the mitochondrial motility. *Biochem. Biophys. Res. Commun.* **353,** 127–132
39. Chua, J. J., Butkevich, E., Worseck, J. M., Kittelmann, M., Grønborg, M., Behrmann, E., Stelzl, U., Pavlos, N. J., Lalowski, M. M., Eimer, S., Wanker, E. E., Klopfenstein, D. R., and Jahn, R. (2012) Phosphorylation-regulated axonal dependent transport of syntaxin 1 is mediated by a Kinesin-1 adapter. *Proc. Natl. Acad. Sci. U.S.A.* **109,** 5862–5867
40. Holleran, E. A., Ligon, L. A., Tokito, M., Stankewich, M. C., Morrow, J. S., and Holzbaur, E. L. (2001) βIII spectrin binds to the Arp1 subunit of dynactin. *J. Biol. Chem.* **276,** 36598–36605
41. Muresan, V., Stankewich, M. C., Steffen, W., Morrow, J. S., Holzbaur, E. L., and Schnapp, B. J. (2001) Dynactin-dependent, dynein-driven vesicle transport in the absence of membrane proteins: a role for spectrin and acidic phospholipids. *Mol. Cell* **7,** 173–183
42. Lorenzo, D. N., Li, M. G., Mische, S. E., Armbrust, K. R., Ranum, L. P., and Hays, T. S. (2010) Spectrin mutations that cause spinocerebellar ataxia type 5 impair axonal transport and induce neurodegeneration in *Drosophila*. *J. Cell Biol.* **189,** 143–158
43. Denisenko, N., Cifuentes-Diaz, C., Irinopoulou, T., Carnaud, M., Benoit, E., Niwa-Kawakita, M., Chareyre, F., Giovannini, M., Girault, J. A., and Goutebroze, L. (2008) Tumor suppressor schwannomin/merlin is critical for the organization of Schwann cell contacts in peripheral nerves. *J. Neurosci.* **28,** 10472–10481
44. Schulz, A., Kyselyova, A., Baader, S. L., Jung, M. J., Zoch, A., Mautner, V. F., Hagel, C., and Morrison, H. (2014) Neuronal merlin influences ERBB2 receptor expression on Schwann cells through neuregulin 1 type III signalling. *Brain* **137,** 420–432
45. Denisenko-Nehrbass, N., Goutebroze, L., Galvez, T., Bonnon, C., Stankoff, B., Ezan, P., Giovannini, M., Faivre-Sarrailh, C., and Girault, J. A. (2003) Association of Caspr/paranodin with tumour suppressor schwannomin/merlin and β1 integrin in the central nervous system. *J. Neurochem.* **84,** 209–221
46. Menegoz, M., Gaspar, P., Le Bert, M., Galvez, T., Burgaya, F., Palfrey, C., Ezan, P., Arnos, F., and Girault, J. A. (1997) Paranodin, a glycoprotein of neuronal paranodal membranes. *Neuron* **19,** 319–331
47. Lonigro, A., and Devaux, J. J. (2009) Disruption of neurofascin and gliomedin at nodes of Ranvier precedes demyelination in experimental allergic neuritis. *Brain* **132,** 260–273
48. He, M., Abdi, K. M., and Bennett, V. (2014) Ankyrin-G palmitoylation and βII-spectrin binding to phosphoinositide lipids drive lateral membrane assembly. *J. Cell Biol.* **206,** 273–288
49. Liu, W., and Devaux, J. J. (2014) Calmodulin orchestrates the heteromeric assembly and the trafficking of KCNQ2/3 (Kv7.2/3) channels in neurons. *Mol. Cell. Neurosci.* **58,** 40–52
50. Traka, M., Goutebroze, L., Denisenko, N., Bessa, M., Nifli, A., Havaki, S., Iwakura, Y., Fukamauchi, F., Watanabe, K., Soliven, B., Girault, J. A., and

Karagogeos, D. (2003) Association of TAG-1 with Caspr2 is essential for the molecular organization of juxtaparanodal regions of myelinated fibers. *J. Cell Biol.* **162,** 1161–1172

51. de Medinaceli, L., Freed, W. J., and Wyatt, R. J. (1982) An index of the functional condition of rat sciatic nerve based on measurements made from walking tracks. *Exp. Neurol.* **77,** 634–643
52. Ozmen, S., Ayhan, S., Latifoğlu, O., and Siemionow, M. (2002) Stamp and paper method: a superior technique for the walking track analysis. *Plast. Reconstr. Surg.* **109,** 1760–1761
53. Goutebroze, L., Carnaud, M., Denisenko, N., Boutterin, M. C., and Girault, J. A. (2003) Syndecan-3 and syndecan-4 are enriched in Schwann cell perinodal processes. *BMC Neurosci.* **4,** 29